CANCER

Respiratory delivery of single low-dose nebulized PFCE-C25 NEs for lymphatic transport and durable stimulation of antitumor immunity in lung cancer

Rong A[1,2]†, Zhaoguo Han[1,2]†, Meifang Zhou[1,2]†, Chaoqun Nie[1,2]†, Mengyuan Zhu[1,2], Sijie Cheng[1,2], Tianyi Wang[1,2], Jing Wang[1,2], Zhen Quan[1,2], Kaiqi Wang[1,2], Shanshan Liu[1,2], Xinxin Hu[1,2], Haoyu Wang[1,2], Jiannan Wang[1,2], Yongyi Wu[1,2], Xilin Sun[1,2]*

The currently available immune checkpoint inhibitors (ICIs) often fail to achieve the desired clinical outcomes due to inadequate immune activation, particularly in patients with lung cancer. To reverse this situation, we synthesized inhalable PFCE-C25 nanoemulsions (NEs), which target lymphocyte activation genes (LAG-3) on immune cells within tumor microenvironment and tumor-draining lymph nodes (TDLNs). By combining in vivo ^{19}F-MR molecular imaging, we investigate the immunological effects of a single low-dose PFCE-C25 NEs in multiple murine lung cancer models, including human immune system (HIS) mouse models, and validated its immunological effects in human TDLNs. The nebulization therapy with PFCE-C25 NEs demonstrated a notable and enduring maturation of dendritic cells (DCs) in TDLNs, leading to systemic immune responses, prolonged survival, the establishment of immune memory, and resistance to tumor rechallenge. Thus, PFCE-C25 NEs successfully demonstrate a promising and efficient approach for enhancing lymphatic transport and sustained activation of antitumor immune responses in lung cancer.

INTRODUCTION

Among all cancers, lung cancer is the most prevalent and the leading cause of cancer-related death, posing a serious public health burden (*1*). Immunotherapy, such as programmed cell death protein 1 (PD-1) or its ligand (PD-L1), and other immune checkpoint inhibitors (ICIs) used to improve T cell activity, has markedly changed the landscape of cancer therapy; however, there are still a substantial number of lung cancer patients who are unresponsive to PD-1/PD-L1 immunotherapy due to insufficient immune activation. The immunosuppressive features include but are not limited to reduced DC maturation, reduced T cell priming, and regulatory T cell (T_{reg}) accumulation (*2*, *3*). LAG-3 has been regarded as an indicator of tumor malignancy and has become a novel tumor immunotherapy target. As a negative regulator of activated T cells, LAG-3 is mostly expressed on the surface of activated cytotoxic $CD8^+$ T cells, activated or exhausted effector $CD4^+$ T cells, B cells, natural killer (NK) cells, DCs, and T_{regs}. T_{regs} can indirectly inhibit the activation of effector T (T_{eff}) cells by suppressing the function of antigen-presenting cells, which are essential for T_{eff} activation and play a crucial role in the adaptive immune response (*4*). Studies have demonstrated that blocking LAG-3 can lead to various immune effects, including the inhibition of T_{reg} function, the enhancement of DC maturation, and the restoration of dysfunctional $CD4^+$/$CD8^+$ T cells (*5*–*7*). Currently, LAG-3 is mainly used in combination therapy with PD-1/PD-L1 to maximize its activation in the treatment of lung cancer. Consequently, the utilization of drug combinations results in not only an inevitable escalation of treatment expenses due to the requirement of a substantial quantity of antibodies but also a greater incidence of adverse effects than single-agent immunotherapies. Therefore, an ideal immunotherapy approach should deliver immunotherapeutic agents efficiently, generate long-lasting and targeted antitumor immune responses, and minimize side effects and treatment costs.

The lungs, which are a respiratory organ, play an important role in the body's immune response. The clearance of therapeutic drugs entering the body via the respiratory tract occurs through the lymph nodes within the lungs, thereby suggesting the substantial potential for immune activation. Moreover, the lungs also have favorable characteristics for drug delivery, including a substantial surface area, abundant blood circulation, and a thin layer of epithelial cells, thus offering promising opportunities for the effective implementation of immune interventions via inhalation of immunotherapeutic medications (*8*). In comparison to intravenous administration and other alternative administration routes, pulmonary delivery could effectively eliminate the migration of drugs through the gastrointestinal tract and avert hepatic first-pass metabolism, thereby increasing the drug bioavailability and minimizing off-target effects. This approach demonstrates promise for the infiltration of immunotherapeutic drugs into lymph nodes and lung tumors, thereby effectively enhancing immune activation and improving the efficacy of immunotherapy for lung cancer while reducing undesired side effects in comparison to intravenous administration (*9*). However, pulmonary delivery is generally unsuitable for conventional formulations, such as liquid drugs, tablets, and capsules. Consequently, the development of a safe and effective drug carrier platform is imperative to facilitate efficient pulmonary drug delivery. The membrane-coated perfluoro-15-crown-5-ether (PFCE) nanoemulsions (NEs) can be stably nebulized; this emulsion has high bioinertness, biocompatibility, and drug-carrying capacity and can serve as an optimal platform for the development of pulmonary targeted delivery systems. Because of the large amount of fluorine atoms in PFCE, ^{19}F-magnetic resonance (MR)–targeted molecular imaging allows the precise visualization and monitoring of tumors without background signal interference (*10*). In addition, our

[1]Department of Nuclear Medicine, the Fourth Hospital of Harbin Medical University, Harbin, China. [2]NHC Key Laboratory of Molecular Probe and Targeted Diagnosis and Therapy, Molecular Imaging Research Center (MIRC) of Harbin Medical University, Harbin, China.
*Corresponding author. Email: sunxl@ems.hrbmu.edu.cn
†These authors contributed equally to this work.

previous study has shown that nebulized PFCE emulsion could efficiently penetrate lung tumor-draining lymph nodes (TDLNs) (*11*). Thus, exploring the impact of the PFCE immunotherapeutic drug carrier platform on systemic immune responses and TDLNs, as well as its potential to enhance treatment outcomes, presents a unique area of inquiry in the field of immunotherapy.

C25 is a cyclic peptide composed of nine amino acids that demonstrates specific binding affinity to both human and mouse LAG-3 protein. By occupying the key binding site of major histocompatibility complex class II (MHC-II), C25 effectively inhibits the LAG-3 signaling pathway results in promising antitumor effects (*12*). Here, we synthesized the inhalable nanomedicine PFCE-C25 NEs, which target LAG-3, based on PFCs, and further explored its ^{19}F imaging properties. The immunotherapeutic efficacy of PFCE-C25 NEs was tested in orthotopic lung cancer models, including HIS mouse models, and the targeting ability and immunological effects of PFCE-C25 NEs were also explored on human TDLN (hTDLN) specimens (Fig. 1). To the best of our knowledge, few studies have explored the treatment effectiveness of cost-effective cyclic peptide– and PFC-based nebulized nanomedicines with excellent LAG-3–targeting capability. Therefore, this strategy is expected to lead to the development of a novel LAG-3 inhibition therapy for clinical lung cancer patients.

RESULTS

PFCE-C25 NEs harboring the anti–LAG-3 drug C25 and exhibiting ^{19}F-MR imaging capabilities were successfully synthesized

As shown by dynamic light scattering (DLS), the hydrodynamic particle size of the PFCE-C25 NEs was approximately 179 ± 14.9 nm, with a polydispersity index (PDI) value of 0.18 ± 0.04 (Fig. 2A). The transmission electron microscopy (TEM) results of the PFCE-C25 NEs revealed a spherical or quasispherical morphology with a uniform distribution (Fig. 2B). Cryogenic TEM (cryo-TEM) images showed a clear core-shell structure for the PFCE-C25 NEs (Fig. 2C). Elemental mapping analysis of the PFCE-C25 NEs also confirmed the compositions of F, O, C, N, and P (Fig. 2D). The ultraviolet-visible (UV-Vis) spectra of C25 peptides at different concentrations presented the same absorption peak at 275 nm (Fig. 2E). Compared with PFCE NEs, the PFCE-C25 NEs exhibited an absorption peak at 275 nm, indicating that the C25 peptide was successfully conjugated. Lissamine rhodamine B sulfonyl–labeled PFCE NEs and PFCE-C25 NEs both displayed similar observation peaks at 570 nm (Fig. 2F). In addition, there were no obvious changes in the diameter or ζ potential of PFCE-C25 NEs at 4°, 25°, or 37°C within 45 days, indicating the excellent stability of the PFCE-C25 NEs (Fig. 2G and fig. S1A). To further explore the stability of PFCE-C25 NEs, we further determined the stability of PFCE-C25 NEs in bronchoalveolar lavage fluid (BALF) solution, phosphate-buffered saline (PBS), and normal saline at different time intervals (1, 3, 5, 8, and 15 days). As shown in fig. S1 (B to D), no notable changes in the hydrodynamic diameters of PFCE-C25 NEs were observed in BALF, PBS, and saline solution at different time intervals. No marked changes in PDI (<0.30; fig. S1, E to G) are detected even after 15 days of storage, suggesting the good stability of PFCE-C25 NEs. Moreover, the findings from the ^{19}F-MR imaging (MRI) and ^{1}H-MRI of PFCE-C25 NEs at varying concentrations revealed the excellent ^{19}F signal properties of PFCE-C25 NEs, and the signal-to-noise ratio (SNR) increased as the probe concentration increased (Fig. 2, H and I).

PFCE-C25 NEs exhibited optimal targeting capability and elicited significant immunological responses

Since C25 specifically binds to both human and mouse LAG-3 and given the fact that LAG-3 is expressed on most immune cells including activated T cells, NK cells, and plasmacytoid DCs, we tested the binding ability and imaging properties of PFCE-C25 NEs on immune cell–enriched hTDLN biopsy samples (Fig. 3A). On the basis of the analysis of the ^{19}F SNR, it is evident that the ^{19}F signal observed in the PFCE-C25 NE–treated group was significantly higher than that in the PFCE NE–treated group ($P < 0.001$; Fig. 3B). The figure presented in Fig. 3C displays the hematoxylin and eosin (H&E) image of hTDLN for different groups from the same patient with stage II lung cancer. The ex vivo fluorescence imaging results strongly corroborate the

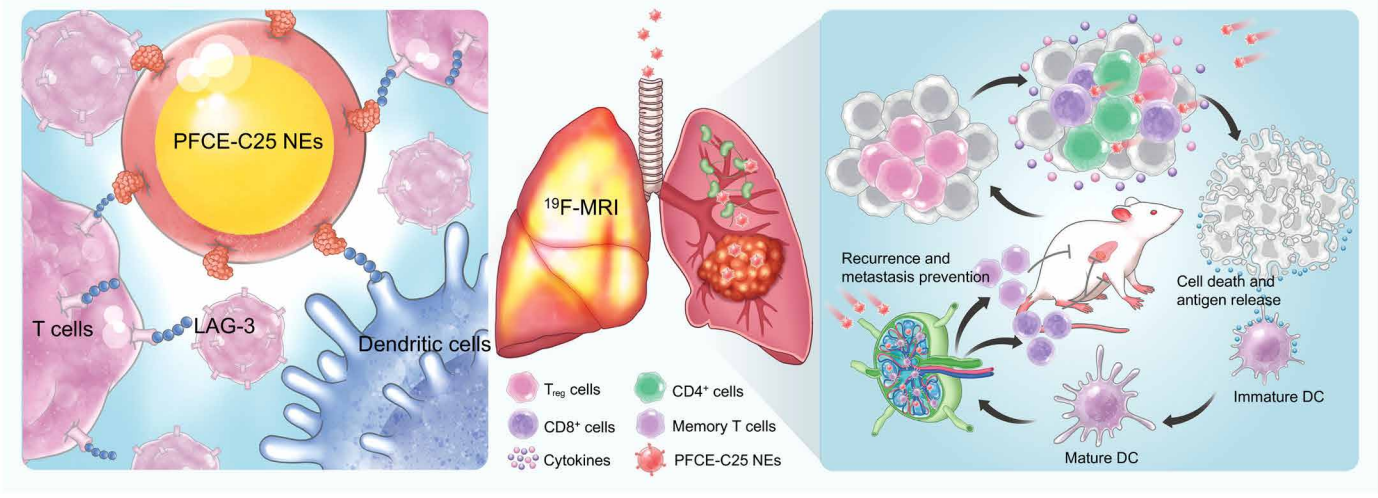

Fig. 1. Schematic illustration of the single low-dose nebulization delivery of PFCE-C25 NE activating lymph nodes and durably stimulating antitumor immunity in lung cancer. The nebulization therapy using PFCE-C25 NEs successfully delivered the LAG-3–targeting therapeutic peptide (C25) to both in situ lung tumors and lung TDLNs, leading to the induction of robust antitumor immune responses and suppression of primary and distant tumor growth. The efficacy of ^{19}F-MR targeting imaging with PFCE-C25 NEs additionally demonstrated the potential of PFCE-C25 NEs as an integrated platform for therapeutic and diagnostic applications in lung cancer nebulization therapy.

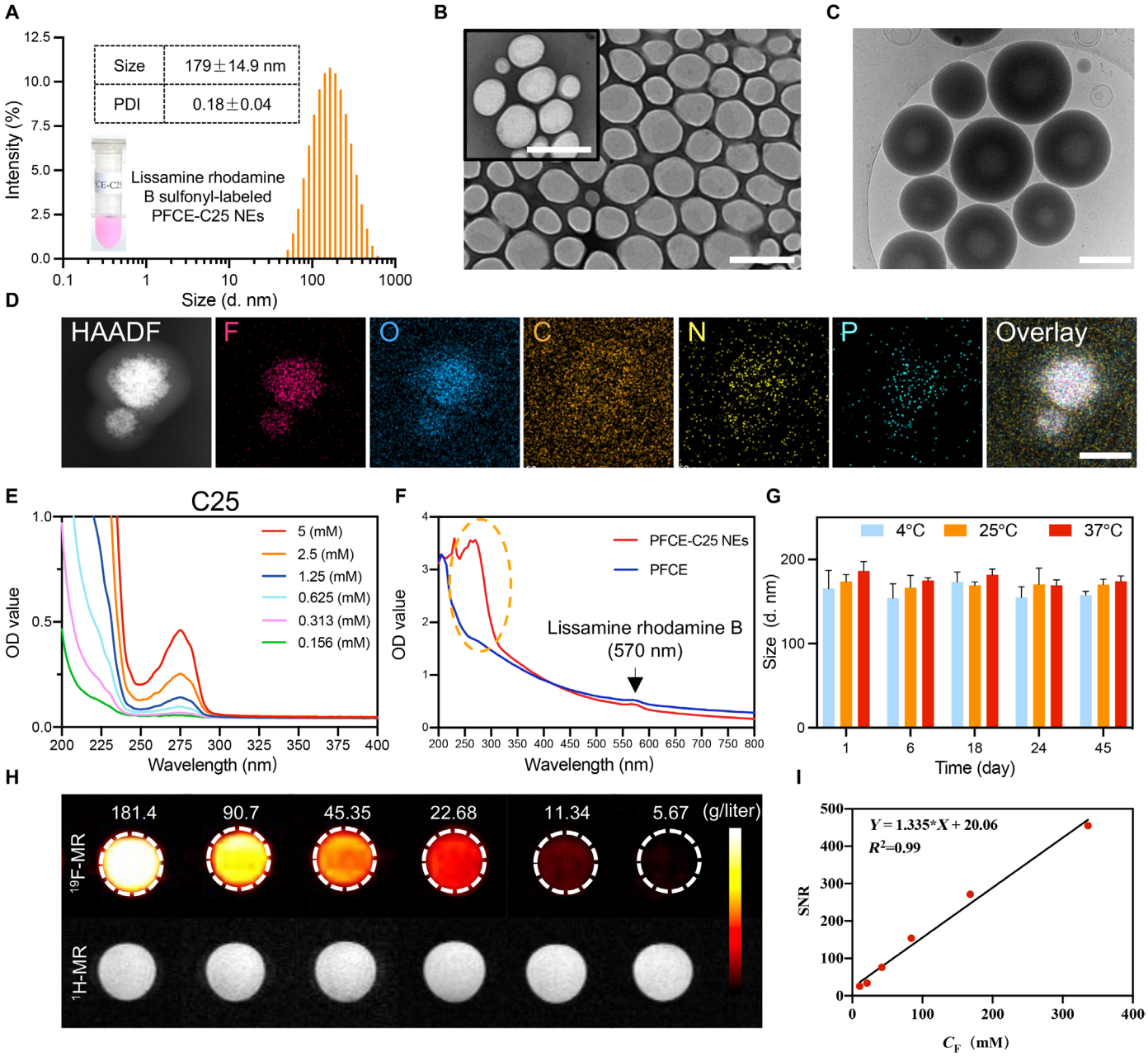

Fig. 2. Characterization of PFCE-C25 NEs. (**A**) Intensity-weighted size distribution of PFCE-C25 NEs. (**B**) Morphology of PFCE-C25 NEs determined by TEM. Scale bars, 500 nm. (**C**) Cryo-TEM images of PFCE-C25 NEs. Scale bar, 200 nm. (**D**) Elemental mapping analysis of PFCE-C25 NEs. Scale bar, 100 nm. (**E**) UV-Vis absorption spectra of C25 cyclic peptides. (**F**) UV-Vis absorption spectra of the PFCE-C25 NEs and PFCE NEs. (**G**) Measurement of changes in the intensity-averaged hydrodynamic diameter size of PFCE-C25 NEs. Three-dimensional (3D) graphs were generated using Matlab based on the average values obtained. (**H**) ^{19}F-MRI and ^{1}H-MRI results of PFCE-C25 NEs. (**I**) Calculation of the SNR of PFCE-C25 NEs at different concentrations. The data are presented as the mean ± SD.

findings of ^{19}F-MRI that the fluorescence signal observed in the PFCE-C25 NE–treated group was significantly higher than that in the PFCE NE–treated group ($P < 0.05$; Fig. 3D). Moreover, flow cytometry analysis revealed that PFCE-C25 NEs considerably enhanced the ratio of CD8$^+$ interferon-γ–positive (IFN-γ$^+$) T and CD4$^+$ IFN-γ$^+$ T cells in the PFCE-C25-NE–treated group compared to the control groups ($P < 0.05$; Fig. 3E). Additionally, the activation level of DCs in human lymph nodes was also enhanced in the PFCE-C25 NE–treated group ($P < 0.01$; Fig. 3F).

In the human peripheral blood mononuclear cell (hPBMC) assay, the IFN-γ production in each T cell subset of hPBMCs was significantly enhanced by PFCE-C25 NE treatment, and the production increased with increasing PFCE-C25 NE concentration. After blocking the LAG-3 protein with the anti–LAG-3 antibody, the PFCE-C25 NEs no longer enhanced IFN-γ release or CD8$^+$ T cell activation (Fig. 3G and fig. S2A). Furthermore, when compared to nonstimulated + PFCE-C25 NEs and stimulated + blocking + PFCE-C25 NEs, the stimulated CD8$^+$ T_{eff} cells demonstrated a robust fluorescence signal

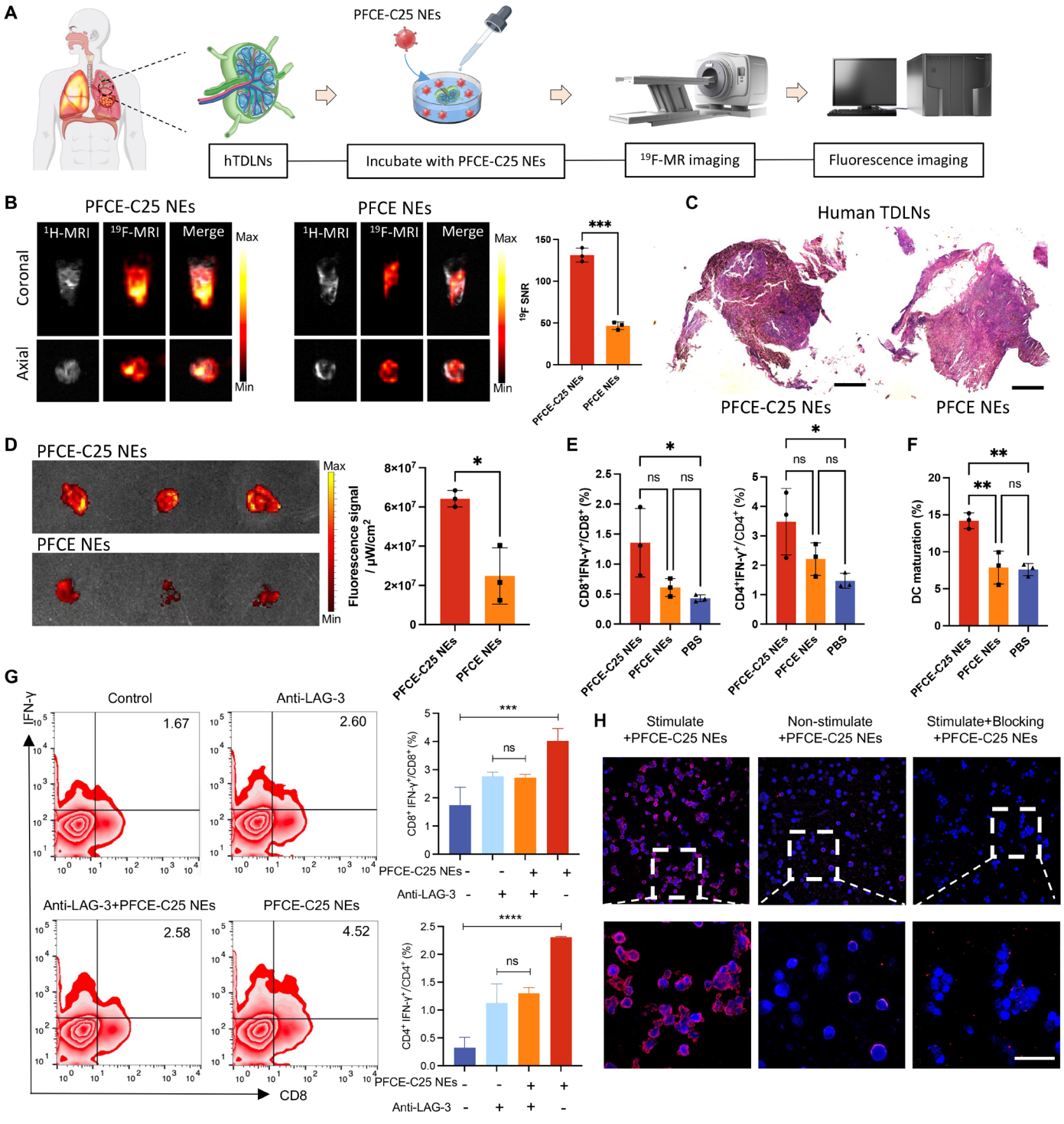

Fig. 3. The targeting and immune function of PFCE-C25 NEs in hTDLNs, hPBMCs, mCD8$^+$ T cells, and lung tumor cells. (**A**) Schematic illustration of hTDLN assay. (**B**) The ^{1}H/^{19}F MR images of hTDLNs were obtained after a 6-hour incubation with PFCE-C25 NEs or PFCE NEs (coronal and axial view). (**C**) Representative H&E staining results of the hTDLN in each group. Scale bar, 20 μm. (**D**) Representative IVIS imaging results of hTDLNs after incubation with PFCE-C25 NEs or PFCE NEs and the corresponding fluorescence signal analysis ($n = 3$). (**E**) Ability of PFCE-C25 NEs to stimulate the secretion of IFN-γ and increase the percentage of CD8$^+$ IFN-γ$^+$ T cells and CD4$^+$ IFN-γ$^+$ T cells in hTDLNs ($n = 3$). (**F**) Comparison of DC activation in hTDLNs from the PFCE-C25 NE–, PFCE NE–, and PBS-treated groups after 6 hours ($n = 3$). (**G**) Ability of PFCE-C25 NEs to stimulate the secretion of IFN-γ by hPBMCs and increase the percentage of CD8$^+$ IFN-γ$^+$ T cells and CD4$^+$ IFN-γ$^+$ T cells ($n = 3$). (**H**) Confocal fluorescence microscopy results of mCD8$^+$ T cells after incubation with PFCE-C25 NEs or PFCE NEs for 4 hours. Magnification scale bar, 20 μm. The data are presented as the mean ± SD.

following exposure to lissamine rhodamine B sulfonyl–labeled PFCE-C25 NEs, indicating the excellent binding capability of PFCE-C25 NEs for LAG-3$^+$ cells. The expression of LAG-3 on CD8$^+$ T cells was enhanced using anti-CD3 and anti-CD28 antibodies, while a LAG-3 blocking antibody was used as a negative control to block LAG-3 on CD8$^+$ T cells (Fig. 3H). Moreover, cell viability was evaluated by MTT assay. Expectedly, the PFCE-C25 NEs did not have pronounced killing effects on Lewis lung carcinoma (LLC), CMT167, or NCI-H460 lung cancer tumor cells (fig. S2B). Therefore, it can be inferred that PFCE-C25 NEs function by immune cell activation.

Single low dose of nebulized PFCE-C25 NEs facilitates the distinctive and sustained maturation of DCs in TDLNs

Immunofluorescence staining of PFCE-C25 NEs after inhalation was performed with lissamine rhodamine B sulfonyl–labeled PFCE-C25 NEs, and the results demonstrated that the PFCE-C25 NEs were nearly homogeneously distributed throughout the lung tissue. There was significant accumulation of PFCE-C25 NEs in the LLC tumor region after 6 hours of nebulization (Fig. 4A and fig. S3). Moreover, the PFCE-C25 NEs exhibited a high degree of accumulation in the TDLN (Fig. 4B). In addition to rescuing dysfunctional CD4$^+$/CD8$^+$ T cells and inhibiting T_{reg} activity, blocking LAG-3 activity can also induce the maturation and activation of DCs (*6*, *13*). The maturation of DCs is imperative for providing costimulatory signals to T cells, facilitating the effective activation of naïve T cells (*14*). Therefore, to better investigate the role of PFCE-C25 NEs in DC maturation and activation, we performed flow cytometry to assess monocyte-derived activated DCs within the TDLNs in LLC model and compared them with those in the C25 peptide group. The results demonstrated that the group treated with PFCE-C25 NEs exhibited a significantly greater rate of DC maturation than the group administered the C25 peptide, as observed after a 2-hour period (2 hours, PFCE-C25 NEs versus C25 peptide, $P < 0.01$), which was essential for promoting T cell priming and recruitment. Simultaneously, we explored the long-term effects of PFCE-C25 NEs on the maturation and activation status of DCs. On day 6 after a single low dose of PFCE-C25 NEs, TDLNs were collected to investigate the degree of DC maturation and compare with that in the group receiving a single dose of the C25 peptide. Notably, compared with the single dose of C25 peptide, PFCE-C25 NEs induced greater DC maturation. These comparative analyses suggested that PFCE-C25 NEs play distinctive and sustained roles in DC maturation after a single low dose of administration (6 days, $P < 0.0001$; Fig. 4C). The maturation of DCs in TDLNs was also identified and visualized directly via immunofluorescence staining for confocal microscopy (Fig. 4D).

PFCE-C25 NEs inhibited the growth of metastatic LLC cells by remodeling the immunosuppressive tumor microenvironment

The immunofluorescence staining results demonstrated that LAG-3 was expressed on T cells within LLC tumor tissues (fig. S4A), and the flow cytometry results revealed that the percentages of CD3$^+$ CD8$^+$ LAG-3$^+$ and CD3$^+$ CD4$^+$ LAG-3$^+$ cells were significantly greater in tumors and TDLNs than in the spleen (fig. S4B). The therapeutic effects of single low-dose nebulized therapy with PFCE-C25 NEs (2.685 mg/kg based on C25 cyclic peptide, single dose, intratracheally) were compared with those of C25 peptide (2 mg/kg per day, intraperitoneally), LAG-3 antibody (10 mg/kg per every 3 days, intraperitoneally), and PBS (every 3 days, intraperitoneally) in an in situ lung cancer metastasis mouse model (Fig. 5A). MRI was used to quantitatively evaluate tumor growth by visualizing individual lung metastases, and the results showed that tumor growth was significantly slower in the PFCE-C25 NE single low-dose treatment group than in the C25 peptide, LAG-3 antibody, or PBS treatment groups (Fig. 5B). The imaging data were consistent with the ex vivo examination of lung metastases (Fig. 5C), which revealed that PFCE-C25 NEs markedly inhibited the growth of in situ LLC tumors (PFCE-C25 NEs versus PBS, $P < 0.01$). The C25 peptide also exhibited moderate therapeutic efficacy (C25 peptide versus PBS, $P < 0.05$; Fig. 5D). The H&E staining of lung tissue from each treatment group confirmed that the PFCE-C25 NE–treated group exhibited significantly suppressed tumor growth compared with the other treatment groups, whereas the effect of the LAG-3 antibody was not significant (Fig. 5E). For the long-term survival study, as presented in the Kaplan-Meier survival curves, the mice treated with PFCE-C25 NEs survived for a significantly longer period of time (PFCE-C25 NEs versus PBS, $P < 0.0001$; PFCE-C25 NEs versus LAG-3 antibody, $P < 0.05$; log-rank test; Fig. 5F). The spleen plays a crucial role in immune function by orchestrating innate and adaptive immune responses, potentially offering additional clues to therapeutic response (*15*). Our findings indicate that spleens from the PFCE-C25-NE–treated group exhibited greater weight compared to the remaining three groups (fig. S5, A and B). The body weights of the mice remained almost unchanged during treatment compared to those of the untreated control mice, indicating the limited side effects of PFCE-C25 NE administration (fig. S5C).

We posited that the antitumor effect of PFCE-C25 NEs was due to alterations in the immunosuppressive tumor microenvironment (TME). On day 6, tumor, spleen, and TDLN tissues were collected for flow cytometry analysis. The proportions of CD8$^+$ T cells and CD4$^+$ T cells were significantly greater in the tumor, spleen, and TDLN in the PFCE-C25-NE–treated group (Fig. 6A), demonstrating an activated antitumor immune phenotype. Moreover, flow cytometry data showed that PFCE-C25 NEs considerably depleted the immunosuppressive cellular component T_{regs} in the tumor (Fig. 6B). The ratio of CD8$^+$ IFN-γ^+ T cells in the PFCE-C25-NE–treated group was significantly greater than that in the C25 peptide, LAG-3 antibody, and control groups, while the ratio of CD4$^+$ IFN-γ^+ T cells was not significantly different between the tumor and spleen (Fig. 6C). These results indicated that PFCE-C25 NEs were capable of inhibiting in situ LLC growth mainly via a CD8$^+$ T cell–dependent mechanism. Given the critical role of MHC-I in the activation of CD8$^+$ T cells and the function of MHC-II in the stimulation of CD4$^+$ T cells, we hypothesized that PFCE-C25 NEs may enhance the expression of MHC-I in DCs. We examined the expression levels of both MHC-I and MHC-II in DCs within the TME of LLC and TDLNs across various treatment groups. Tumor tissues and TDLNs were collected on day 6 posttreatment initiation for flow cytometry analysis. The findings revealed a higher percentage of CD11c$^+$ MHC-II$^+$ and CD11c$^+$ MHC-I$^+$ DCs in the PFCE-C25 NE treatment group compared to the other three treatment groups in both the LLC TME and TDLNs. Furthermore, the mean fluorescence intensity (MFI) analysis revealed an up-regulation of both MHC-I and MHC-II expression in the PFCE-C25 NE treatment group, indicating the best therapeutic effects of PFCE-C25 NEs (figs. S6 and S7).

The enzyme-linked immunosorbent assay (ELISA) results revealed that the concentrations of IL-6 and IL-12, which play

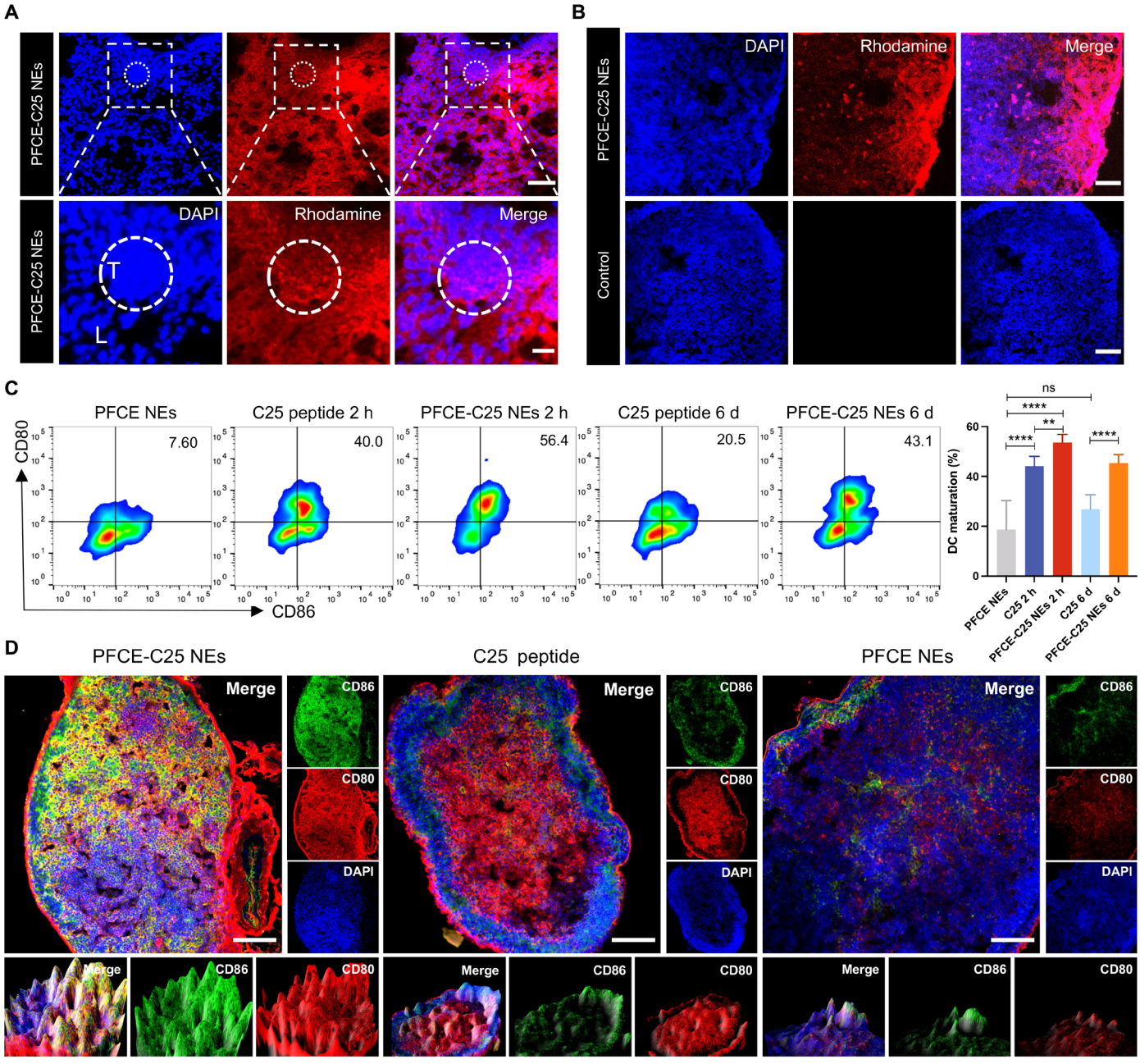

Fig. 4. Distribution of PFCE-C25 NEs in the lung and TDLNs and the activation of DCs. (**A**) Confocal fluorescence microscopy results showing the distribution of PFCE-C25 NEs in lung (L) and LLC tumor (T) tissues. Scale bar, 100 μm (200 μm for magnification). (**B**) Distribution of PFCE-C25 NEs in LLC TDLNs after 6 hours of nebulization delivery of 50 μl of PFCE-C25 NEs. Scale bar, 100 μm. (**C**) Comparison of DC activation in LLC TDLNs from the PFCE NEs, PFCE-C25 NEs, and C25 administration groups after different durations (2 hours, 6 days, $n = 6$). (**D**) Confocal fluorescence microscopy results showing the degree of DC activation in the PFCE NE, PFCE-C25 NE, and C25 administration groups. Scale bar, 100 μm. The data are presented as the mean ± SD.

important roles in activating NK cells, were obviously increased in the lungs of mice treated with PFCE-C25 NEs. The levels of cytokines, including tumor necrosis factor–α (TNF-α) and IFN-γ, were also obviously increased, which further indicated that PFCE-C25 NEs induced stronger cellular immune responses (Fig. 6D). However, on day 6 after initial administration, the concentrations of different cytokines in the serum samples in the PFCE-C25 NE group were nearly similar to those in the PBS group, indicating that a single low dose of nebulized delivery of PFCE-C25 NEs was less likely to induce acute inflammatory responses throughout the entire therapeutic regimen. In contrast, after intraperitoneal administration of the C25 peptide and LAG-3 antibody, the concentration of cytokines in the serum was apparently elevated, which further indicated that the systemic administration of the C25 peptide and LAG-3 antibody induced side effects (Fig. 6E).

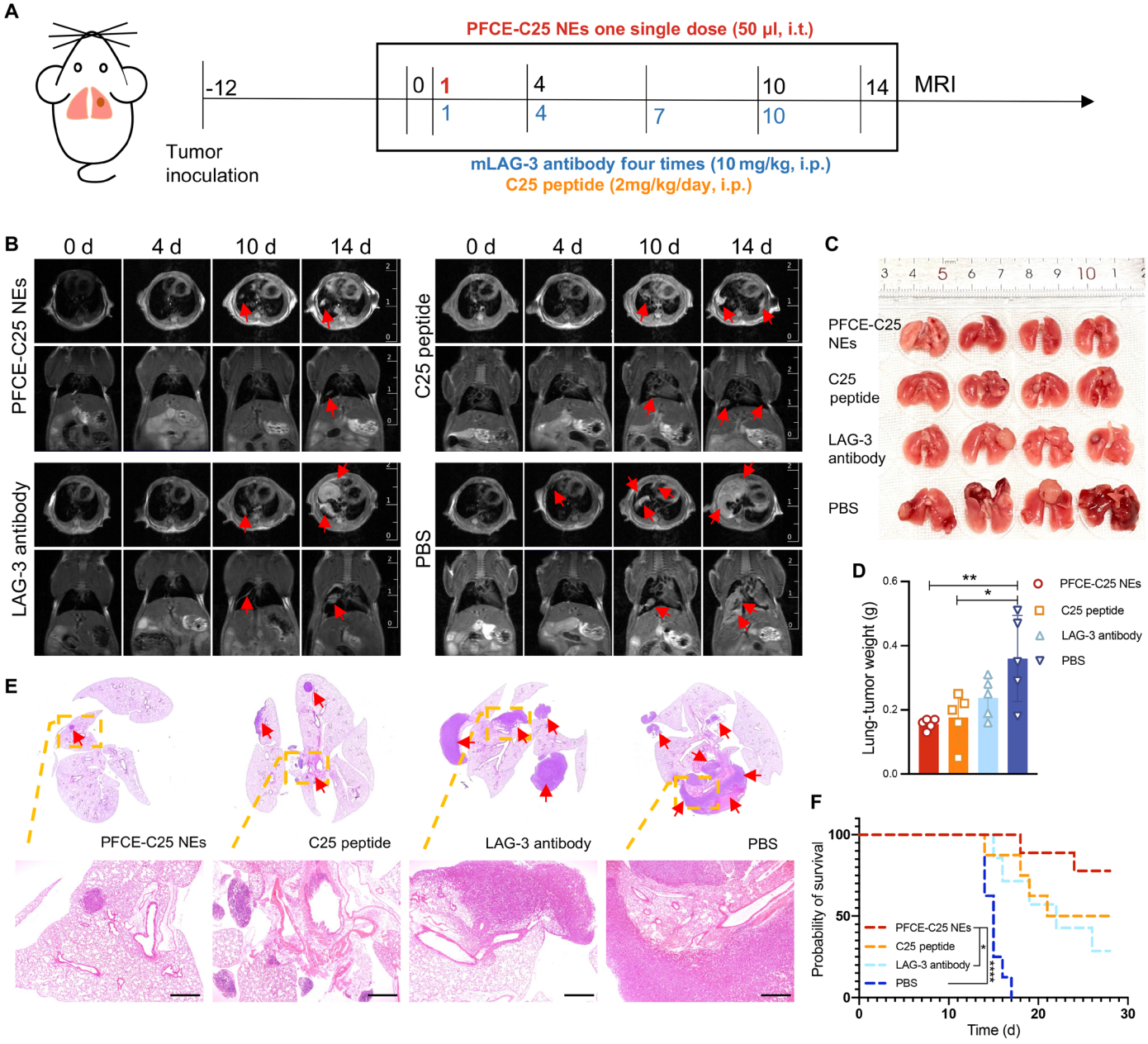

Fig. 5. Therapeutic effect of PFCE-C25 NEs on the LLC metastatic model. (**A**) Schematic diagram of the dosing and imaging regimens for each experimental group. i.t., intratracheally; i.p., intraperitoneally. (**B**) MRI results for immunotherapy monitoring. Red arrow points to the tumor. (**C**) Lung-solid tumor images in each research group. (**D**) Weight statistics of the lung-solid tumors in each group ($n = 5$). The data are presented as the mean ± SD. (**E**) Representative H&E staining results of the lung in each treatment group. Red arrow points to the tumor. Scale bar, 20 μm. (**F**) Log-rank survival curve analysis.

PFCE-C25 NEs inhibited CMT167-induced in situ lung tumor growth by remodeling the immunosuppressive TME

To further demonstrate that our proposed PFCE-C25 NE–based immunotherapy could be broadly applicable, we tested these treatments in an additional murine lung cancer cell model constructed with C57BL/6 mice and CMT167 cells. The LAG-3 expression status in CMT167 orthotopic lung cancer was explored by flow cytometry and immunofluorescence staining (fig. S8A). The flow cytometry results revealed that the percentages of $CD3^+$ $CD8^+$ LAG-3^+ and $CD3^+$ $CD4^+$ LAG-3^+ cells in tumors and TDLNs were significantly greater than those in the spleen (fig. S8B). A schematic of the dosing and imaging schedule is shown in fig. S9A. Moreover, we obtained similar therapeutic results as those for LLC tumors; tumor growth was significantly slower in the PFCE-C25 NE single low-dose treatment group than in the C25 peptide, LAG-3 antibody, and PBS treatment groups. The magnetic resonance anatomical imaging data were consistent with the ex vivo examination of lung metastases, which revealed that PFCE-C25 NEs markedly inhibited the growth of CMT167 orthotopic lung cancer cells (PFCE-C25 NEs versus PBS, $P < 0.0001$). In addition, the C25 peptide also exhibited moderate

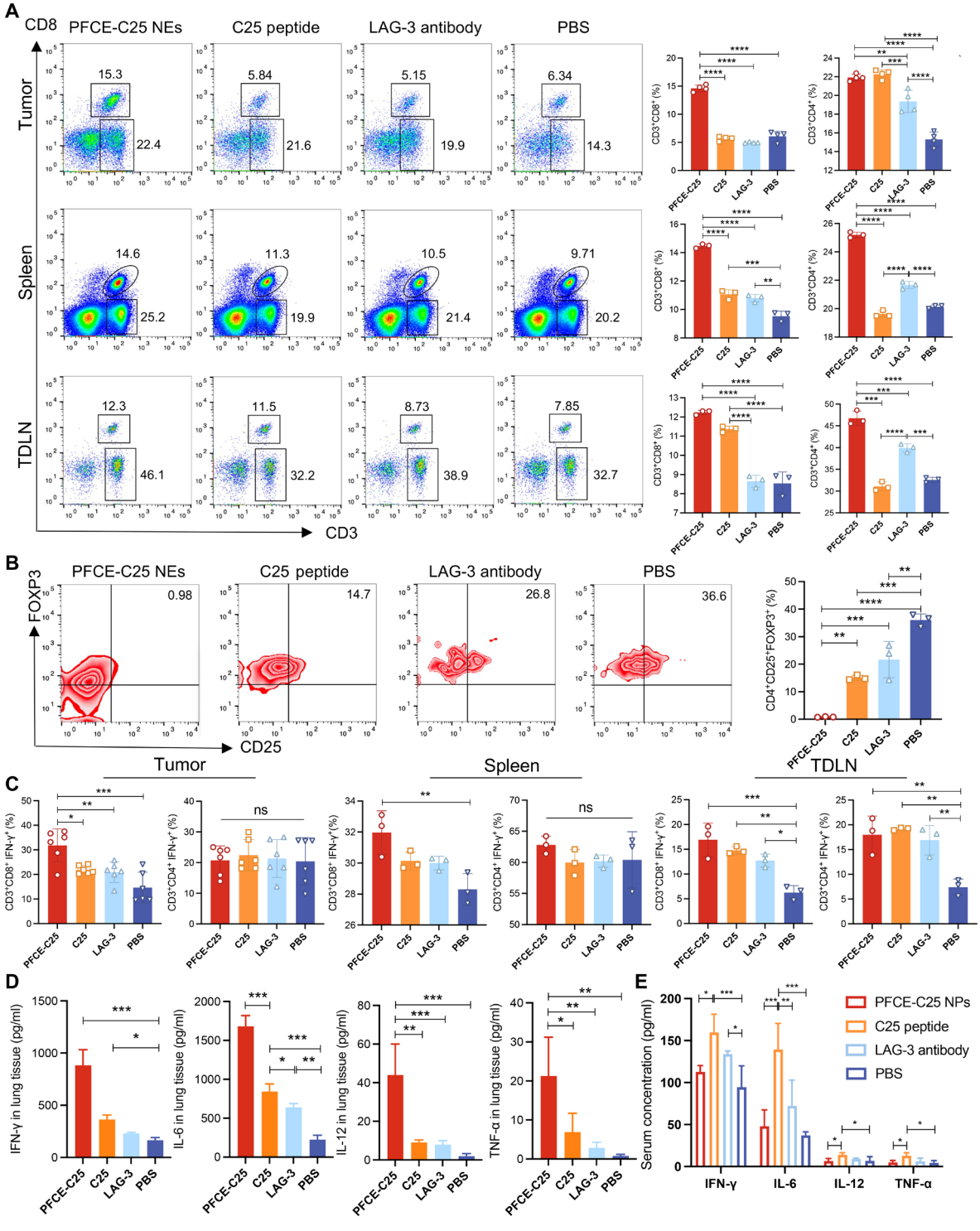

Fig. 6. PFCE-C25 NEs inhibit LLC tumor growth by activating CD8$^+$ T cells, reducing FOXP3$^+$ T_{regs}, and increasing proinflammatory cytokine production. (**A**) CD8$^+$ T cell and CD4$^+$ T cell infiltration in tumors ($n = 4$), spleens ($n = 3$), and TDLNs ($n = 3$). (**B**) FOXP3$^+$ T_{reg} infiltration in tumors of each treatment group ($n = 3$). (**C**) Ratios of CD8$^+$ IFN-γ$^+$ T cells and CD4$^+$ IFN-γ$^+$ T cells in tumors ($n = 6$), spleens ($n = 3$), and TDLNs ($n = 3$) of each treatment group. (**D**) Levels of IFN-γ$^+$, IL-6, IL-12, and TNF-α in tumors. (**E**) The levels of IFN-γ$^+$, IL-6, IL-12, and TNF-α in serum of each treatment group were verified by ELISA ($n = 4$). The data are presented as the mean ± SD.

therapeutic efficacy, which was significantly greater than that of the LAG-3 antibody treatment group (C25 peptide versus PBS, $P < 0.001$; LAG-3 antibody versus PBS, $P < 0.05$; fig. S9, B to D). H&E staining of lung tissue from each treatment group confirmed the above results (fig. S9E). The mice treated with PFCE-C25 NEs survived for a significantly longer period of time (PFCE-C25 NEs versus PBS or LAG-3 antibody, $P < 0.001$, log-rank test; fig. S9F). Moreover, the infiltration of $CD8^+$ IFN-γ^+ T cells, $CD4^+$ IFN-γ^+ T cells, and $FOXP3^+$ T_{regs} into tumors, the spleen and TDLNs in different treatment groups were analyzed after the sixth day of treatment. The results showed that the ratio of $CD8^+$ IFN-γ^+ T cells in the PFCE-C25 NE group was significantly greater than that in the C25 peptide, LAG-3 antibody, and control groups, while the ratio of $CD4^+$ IFN-γ^+ T cells was not significantly different in the TDLNs, indicating that PFCE-C25 NEs inhibit cancer growth mainly via a $CD8^+$ T cell–dependent mechanism (fig. S9G). In addition, flow cytometry data showed that PFCE-C25 NEs considerably decreased T_{reg} numbers (fig. S10). The spleens in the PFCE-C25-NE–treated group were heavier than those in the other three groups ($P < 0.01$; fig. S11, A and B). The weight of the mice remained almost unchanged during the treatment (fig. S11C).

Together, the above results indicated that the immunosuppressive TME in different cell lines was markedly reversed by PFCE-C25 NE treatment, indicating that the nebulized delivery of PFCE-C25 NEs could effectively promote innate and adaptive cell-mediated immune responses.

PFCE-C25 NEs induced T cell–mediated antitumor immune responses

To determine whether the anticancer immune responses caused by PFCE-C25 NEs are related to T cell–mediated adaptive immunity, we next applied an anti-CD4 antibody and an anti-CD8a antibody to deplete T cells in vivo. Before treatment, we depleted T cells by applying antibodies on days 8 and 11 (Fig. 7A). Flow cytometry analysis of the ratio of $CD4^+$ T cells to $CD8^+$ T cells in the serum was carried out to determine whether the corresponding T cells were completely depleted (Fig. 7B). After the successful depletion of T cells, we started PFCE-C25 NE administration. The MRI results demonstrated that tumor growth in both the $CD4^+$ and $CD8^+$ T cell depletion groups occurred faster than that in the PFCE-C25 NE–treated group (Fig. 7C). The body weights of the mice did not significantly change during treatment (Fig. 7D). The decrease in immunotherapy efficacy was

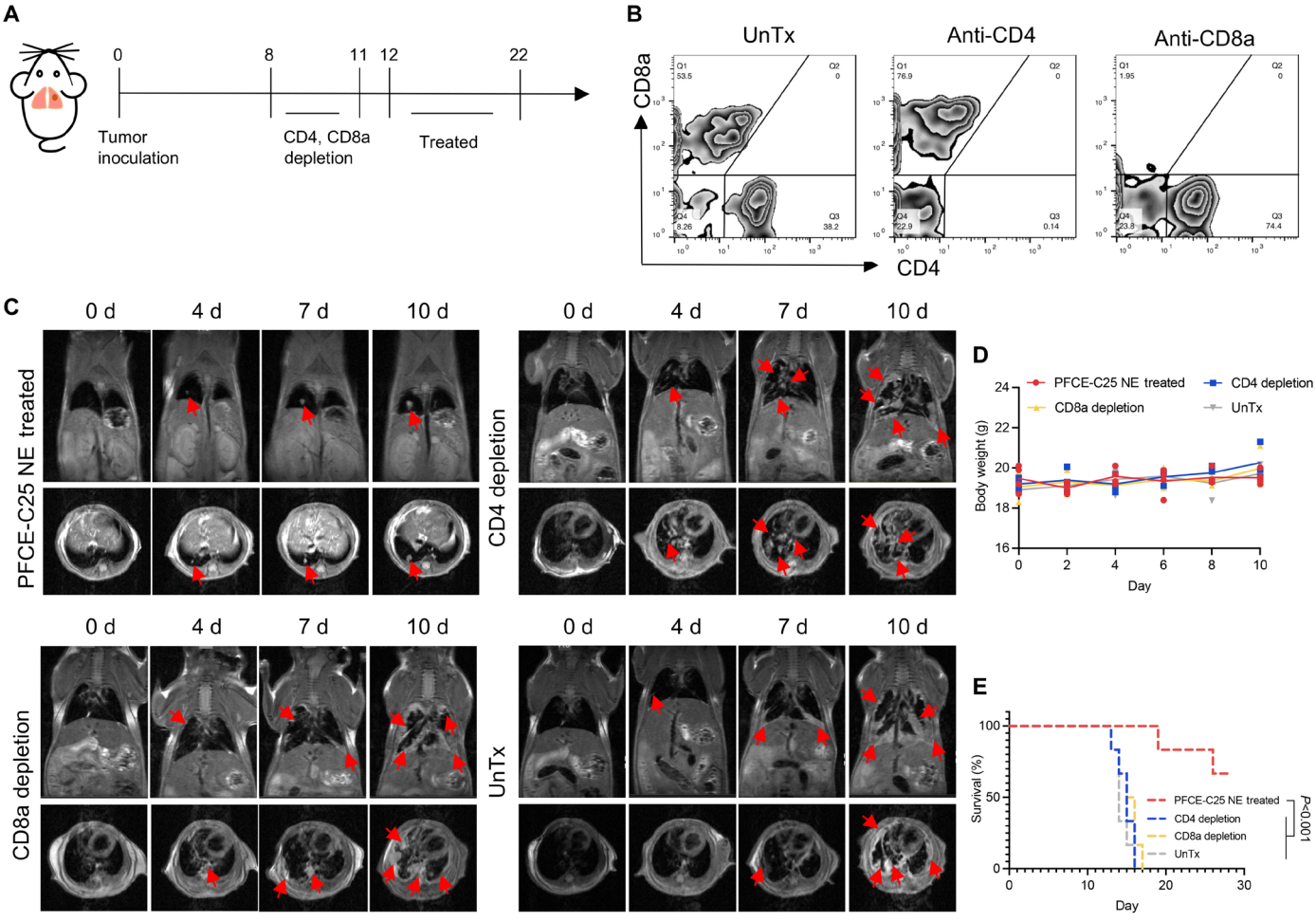

Fig. 7. Effect of PFCE-C25 NEs on an LLC metastatic model after the depletion of $CD8^+$ T cells or $CD4^+$ T cells in mice. (**A**) Schematic diagram of the depletion and treatment regimen. (**B**) Flow cytometry results for $CD8^+$ T cell– or $CD4^+$ T cell–depleted mice. (**C**) MRI results for immunotherapy monitoring. The red arrow points to the tumor. (**D**) Mouse body weight measurements ($n = 3$). (**E**) Log-rank survival curve analysis.

determined by survival analysis and further confirmed the above results (Fig. 7E). These data indicated that T cell–mediated antitumor immune responses are essential for PFCE-C25 NE–based cancer immunotherapy.

PFCE-C25 NEs enhanced local and distant tumor immune responses

The PFCE-C25 NEs significantly inhibited the growth of LLC tumors, and the PFCE-C25 NEs were delivered to TDLNs to promote the maturation of DCs and activation of T cells. Next, we wondered whether local immunotherapy could be sufficient to induce a systemic immune response to suppress the growth of distant tumors. A schematic illustration of the in situ and subcutaneous tumor inoculation methods is shown in Fig. 8A. The MRI results indicated significant regression of tumors in the right armpit region following the administration of PFCE-C25 NE nebulization therapy (Fig. 8B). The subcutaneous tumor growth data demonstrated that the tumors in the right armpit region of the PFCE-C25 NEs completely disappeared by the end of the treatment

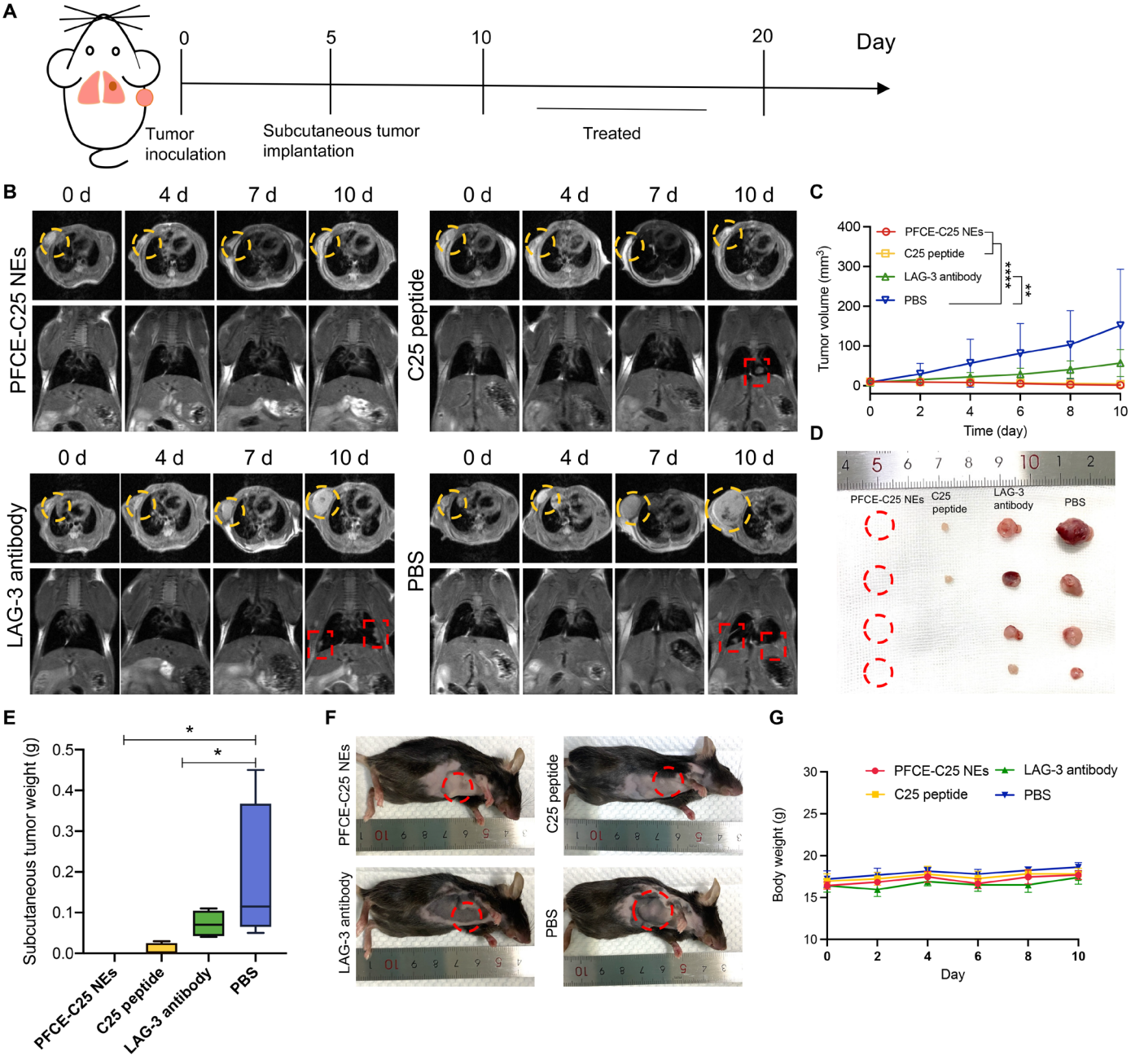

Fig. 8. PFCE-C25 NEs enhance local and distant tumor immune responses. (**A**) Schematic diagram of tumor establishment and the treatment regimen. (**B**) MRI results for immunotherapy monitoring. (**C**) Subcutaneous tumor volume of each treatment group. (**D**) Subcutaneous tumor images of each treatment group. (**E**) Subcutaneous tumor weight of each treatment group. (**F**) Representative mouse images from each treatment group. (**G**) Mouse body weight changes. The data are presented as the mean ± SD; $n = 5$ mice in PFCE-C25 NE and C25 peptide groups; $n = 4$ mice in LAG-3 antibody and PBS groups.

period, indicating that the nebulized delivery of PFCE-C25 NEs induced remarkable systemic antitumor immune responses (Fig. 8, C to F). Notably, the C25 peptide group also exhibited apparent systemic antitumor immune responses, and the subcutaneous tumor weights in the C25 peptide group were significantly lower than those in the LAG-3 antibody treatment and control groups (Fig. 8, D to F). There was no notable difference between the body weights of the control and treated animals (Fig. 8G). While effective, this C25 peptide intervention requires daily intraperitoneal injections. There was no substantial difference in the incidence of orthotopic lung tumors among the other three treatment groups due to the short duration of therapy (fig. S12, A and B). These results intuitively indicated that local administration of PFCE-C25 NEs could markedly induce systemic antitumor immune responses and abscopal effects to promote metastatic tumor regression.

PFCE-C25 NEs induced immune memory in LLC mice

In our study, the treatment was effective in a maximum of 75% of the mice, and a subset of 5 mice (5 of 30, 16.7%) that achieved complete cure and showed no sign of disease for at least 36 days were chosen for flow cytometry analysis. The flow cytometric analysis of blood samples collected on day 37, 2 days before the second tumor was inoculated, showed that the percentages of both central memory T (T_{CM}) cells (T_{CM}; $CD8^+$ $CD44^{high}$ $CD62L^{high}$) and effector memory T (T_{EM}) cells ($CD8^+$ $CD44^{high}$ $CD62L^{low}$) were determined to be 1.46% and 18.9%, respectively. These percentages were higher than those of the C25 peptide and control groups, which were 0.78% and 13.9%, and 0.76% and 10.3%, respectively (PFCE-C25 NEs versus C25 peptide, $P < 0.05$; PFCE-C25 NEs versus untreated, $P < 0.01$; Fig. 9A). In both models, mice with complete responses were rechallenged on day 39 after 14 days of treatment with the same tumor line. Consistent with the development of immunologic memory, the long-term surviving mice resisted secondary tumor challenge compared to age-matched naïve controls engrafted with the same cells, indicating that the PFCE-C25 NE nebulized immunotherapy triggers antitumor memory. As shown in Fig. 9B, a 100% tumor rejection rate was observed in PFCE-C25 NE–treated LLC mice, whereas a 0% tumor rejection rate was observed in naïve mice (Fig. 9B). The H&E staining results for lung tissue 22 days after tumor inoculation are displayed in Fig. 9C. The immunofluorescence staining results of the TDLNs from completely cured mice further demonstrated that the infiltration of PFCE-C25 NEs in the TDLN effectively triggered efficacious immunologic memory (Fig. 9D), which is essential for the immune surveillance of residual and metastatic tumors, long-lasting antitumor immunity, and, ultimately, the control of malignant tumors.

PFCE-C25 NEs exerted significant immunological effects in HIS in situ lung cancer model

To better explore the clinical translational potential of PFCE-C25 NEs, we generated immunodeficient NOG mice repopulated with hPBMCs to study human immune function in vivo. Patients with a frequency of more than 20% of $hCD45^+hCD3^+$ cells were selected for treatment assessment (Fig. 10A). We observed that, compared with nonreconstructed mice, successfully reconstructed HIS mice produced larger spleens due to immune cell infiltration. In addition, hLAG-3 expression on T cells within NCI-H460 in situ lung tumors from a HIS mouse model was assessed by flow cytometry and immunofluorescence staining (Fig. 10B and fig. S13). The flow cytometry results showed that $CD8^+$ T cells in tumors expressed more hLAG-3 than did those in the spleen, and even higher expression levels were observed for $CD4^+$ and $CD8^+$ T cells from the TDLN (Fig. 10B). Additionally, we observed therapeutic results similar to those observed in LLC and CMT167 lung tumor-bearing mice, in which PFCE-C25 NE single low-dose nebulization therapy displayed excellent therapeutic efficacy compared with the C25 peptide, LAG-3 antibody, and PBS treatment groups. T_1WI anatomical MRI results revealed that the tumor size gradually decreased in the PFCE-C25 NE treatment group under the planned therapy regimen compared with the other groups (Fig. 10, C and D). Furthermore, the most significant increases in $CD8^+$ T cell activation and percentage in NCI-H460 lung tumors and in the TDLN were observed in HIS mice treated with PFCE-C25 NEs (Fig. 10, E and F, and fig. S14). H&E staining of lung tissue from each treatment group validated the above results (Fig. 10G and fig. S15). The evaluation of lung tumor weight also confirmed the excellent immunotherapeutic effects of PFCE-C25 NEs (fig. S16A). There was no remarkable difference in the body weight of the mice among the treatment groups (fig. S16B). Together, the above results demonstrated that a single low dose of nebulization therapy with PFCE-C25 NEs could significantly inhibit in situ tumor growth in NCI-H460–bearing HIS mice and promote $CD8^+$ T cell infiltration into tumors and TDLNs to exert antitumor immunotherapeutic effects.

PFCE-C25 NEs exhibited optimal distribution, cytotoxicity, and biocompatibility properties

Following the nebulization delivery of PFCE-C25 NEs at various time intervals (1, 3, 7, and 14 days), the mice were euthanized, and the primary tissues were subsequently collected and examined using IVIS. The fluorescence signals were exclusively detected in the pulmonary region (fig. S17, A and B). Furthermore, the ^{19}F MRI signal persisted in the lungs even on day 14 after a single low dose of PFCE-C25 NEs was administered (fig. S18, A and B). Moreover, tumor tissues and major organs were collected for the quantification of PFCE content via ^{19}F-NMR (nuclear magnetic resonance) at various time points (2 hours, 1 day, 6 days, and 14 days). The findings indicated that nebulized PFCE-C25 NEs primarily accumulated in the lung, LLC tumor, and TDLN (fig. S19A). The corresponding C25 content in each organ was calculated (fig. S19B). In contrast, the C25 peptide content in tumor tissues and major organs was assessed via high-performance liquid chromatography (HPLC) at different time intervals following intraperitoneal injection of C25 peptides (fig. S19C). The results revealed that the C25 peptide was predominantly distributed in the liver, spleen, and other metabolic organs. The PFCE-C25 NE group had 5.73 times higher C25 peptide concentration in tumor tissue and 1.87 times higher in TDLN tissue compared to the intraperitoneal injection of the C25 peptide group after 2 hours. The comparative statistical findings pertaining to the C25 content in tumors indicate that the C25 peptide undergoes rapid metabolism. Thus, after 24 hours of injection, the concentration of the C25 peptide in the tumor tissue after C25 peptide injection was 111.52 times lower, and that in the TDLN tissue was 42.17 times lower than that in the PFCE-C25 NE–treated group (fig. S19D). Compared with intraperitoneal injection of the C25 peptide, PFCE-C25 NEs demonstrated a slower metabolic rate, as indicated by the presence of the peptide in the lung, tumor, and TDLN even 14 days after injection. These outcomes highlight the substantial enhancement in drug retention within the targeted site through the nebulized delivery of PFCE-C25 NEs.

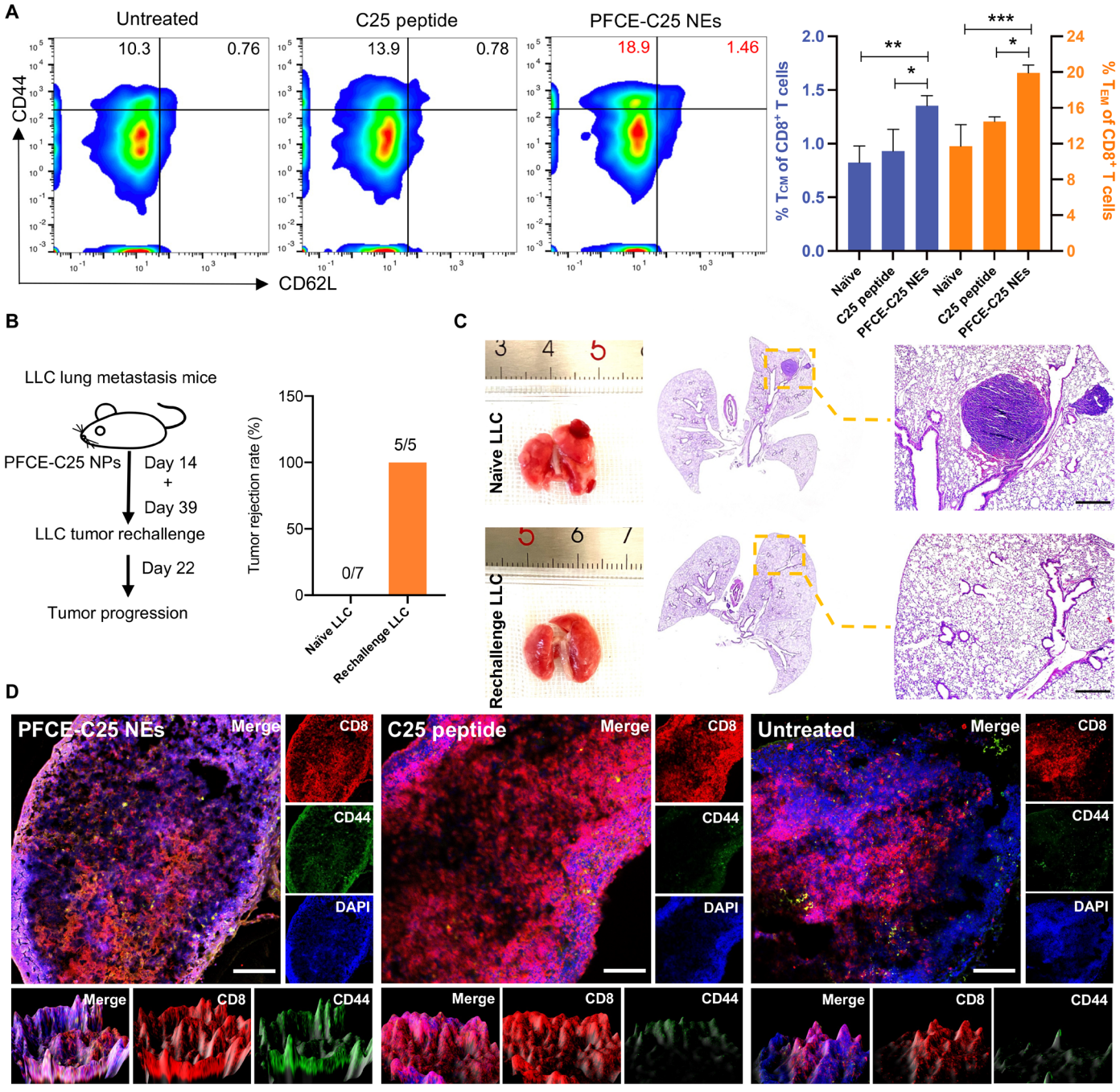

Fig. 9. PFCE-C25 NEs induce immune memory. (**A**) Flow cytometry results showing the percentages of T_{CM} cells ($CD8^+$ $CD44^{high}$ $CD62L^{high}$) and T_{EM} cells ($CD8^+$ $CD44^{high}$ $CD62L^{low}$) in C25 cyclic peptide– and PFCE-C25 NE–treated group mice. The results were compared with those of the untreated group. (**B**) Regimen used for tumor rechallenge and corresponding statistics. (**C**) Representative H&E staining results of lungs from naïve LLC and rechallenge LLC groups. Scale bar, 20 μm. (**D**) Confocal fluorescence microscopy results for $CD8^+$ $CD44^+$ T cells in the TDLNs of PFCE NE–, PFCE-C25 NE–, and C25-treated groups. Scale bar, 100 μm. The data are presented as the mean ± SD.

To investigate the uniform distribution of PFCE-C25 NEs within micrometer-sized aerosol droplets after nebulization, samples of nebulized PFCE-C25 NEs and BALF from mice were observed using TEM. TEM results indicate that the nebulizing device maintained the structures of PFCE-C25 NEs and produced micrometer-sized aerosol droplets. Additionally, analysis of BALF showed that the aerosol droplets contained uniform spherical PFCE-C25 NEs following 5 min of nebulization. Subsequent TEM analysis of BALF after 6 hours of nebulization delivery revealed that PFCE-C25 NEs were effectively dispersed and retained their original morphology (fig. S20, A to D). Furthermore, the TEM analysis of tissue revealed that PFCE-C25 NEs effectively penetrated deep tissue, including the alveolar space, alveolar wall, LLC tumor margin, nonnecrotic tumor area, and TDLN. Notably, TEM images successfully captured the interaction between DCs and T cells,

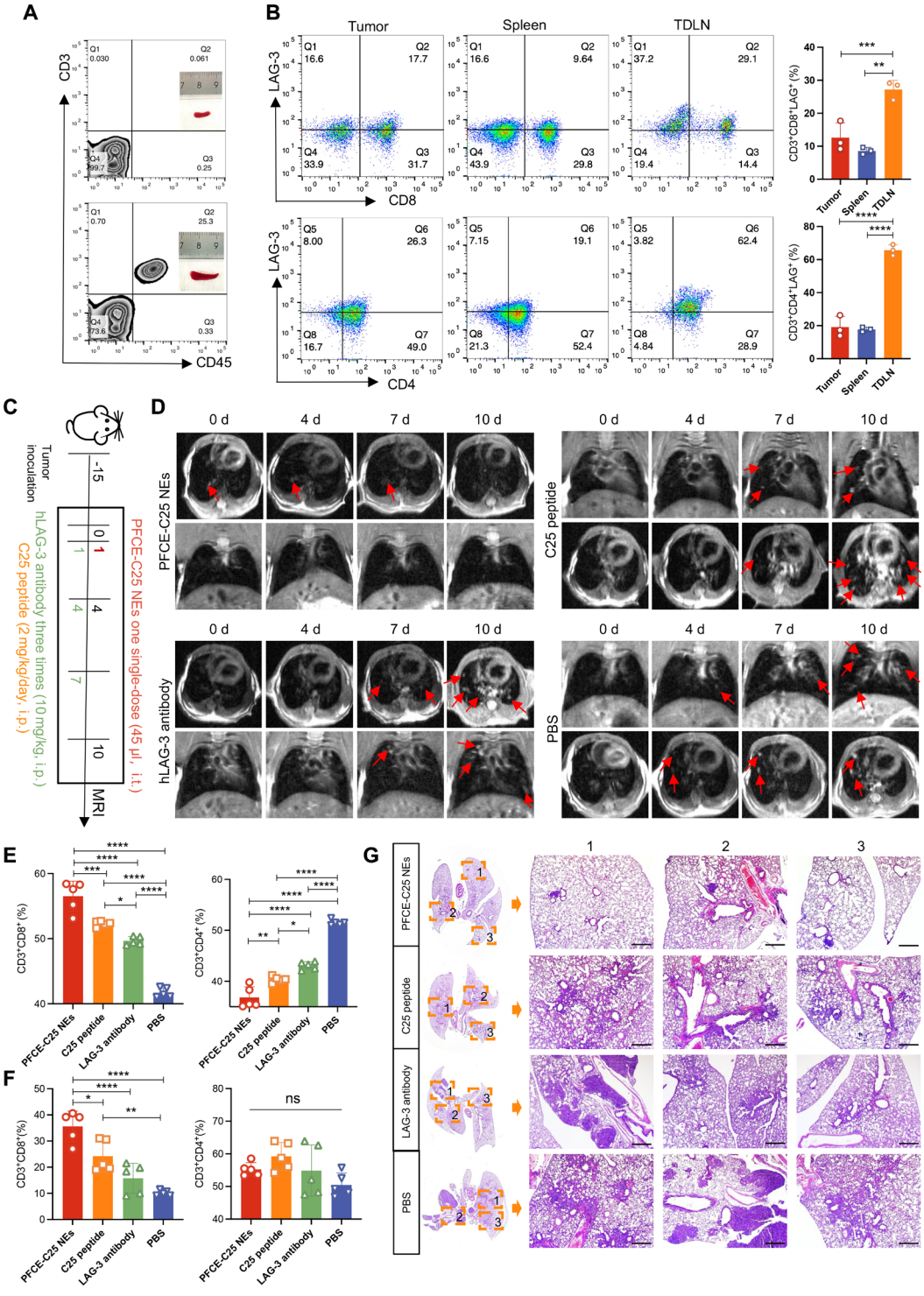

Fig. 10. The immune function of PFCE-C25 NEs in a HIS in situ lung cancer model. (**A**) Flow cytometry results demonstrated the frequencies of hCD45$^+$ hCD3$^+$ cells in PBMCs from immunodeficient NOG mice that were repopulated with hPBMCs (n = 3). Additionally, the spleen size of reconstructed NOG mice was compared to that of nonreconstructed NOG mice. (**B**) Flow cytometry results showing hLAG-3 expression in NCI-H460 in situ lung tumors from a humanized mouse model. (**C**) Schematic diagram of the dosing and imaging regimen for each treatment group. (**D**) MRI results for immunotherapy monitoring. Red arrow points to the tumor. (**E**) CD8$^+$ T cell and CD4$^+$ T cell infiltration into the tumor. (**F**) CD8$^+$ T cell and CD4$^+$ T cell infiltration into the TDLNs; n = 5. The data are presented as the mean ± SD. (**G**) Representative H&E staining results of the lungs of HIS in situ lung cancer mouse model from each treatment group. Scale bar, 20 μm.

visualizing the immune effects facilitated by PFCE-C25 NEs (fig. S20, E to J). Additionally, the fluorescence distribution results of PFCE-C25 NEs in mouse lung tissue demonstrated a uniform distribution following nebulization for a duration of 6 hours (fig. S20, K and L).

The in vivo toxicities of the PFCE-C25 NEs, C25 peptide, and LAG-3 antibody were assessed via histological analysis. The major organs (heart, liver, spleen, lung, and kidneys) were harvested 14 days after injection. Figure S21 shows that the PFCE-C25 NEs, C25 peptide, and LAG-3 antibody did not induce apparent pathological changes, such as cytoplasmic loss, cell atrophy, or inflammation, suggesting excellent biocompatibility. Additionally, a standard biochemical index analysis revealed no changes in blood alanine aminotransferase (ALT), alkaline phosphatase (ALP), or aspartate aminotransferase (AST) levels between the PFCE-C25 NE–treated and saline control groups, demonstrating healthy liver function. Blood urea (UREA) and creatinine (CREA) levels also remained normal in the PFCE-C25-NE–treated group, indicating normal kidney function. Finally, no substantial changes were detected in red blood cells (RBCs), platelets (PLTs), white blood cells (WBCs), mean corpuscular hemoglobin (MCH), mean corpuscular hemoglobin concentration (MCHC), red cell volume distribution width (RDW), platelet-larger cell ratio (P-LCR), procalcitonin (PCT), hemoglobin (HGB), coefficient of variation of RDW, (CV RDW), mean platelet volume (MPV), hematocrit (HCT), mean corpuscular volume (MCV), or platelet distribution width (PDW), revealing that the treatment did not negatively affect the physiological regulation of the immune system in mice (fig. S22).

DISCUSSION

Here, we investigated the efficacy of a single low-dose nebulized PFCE NE harboring the anti–LAG-3 drug C25 in the treatment of lung cancer, and revealed the following key findings: (i) the nebulization delivery of PFCE represents a potentially powerful therapeutic platform for the delivery of the C25 cyclic peptide; (ii) the PFCE-C25 NE therapy achieved the efficient delivery of C25 to TDLNs; (iii) the PFCE-C25 NE nebulization therapy induced robust antitumor immune responses and inhibited in situ primary and distant tumor growth; (vi) the PFCE-C25 NE therapy promoted sustained DC maturation and activation, offering a potential resolution for the inadequate immune response observed in lung cancer; and (v) the PFCE-C25 NE therapy ultimately prolonged the survival of tumor-bearing mice and promoted immune memory development.

Over the past few decades, nebulized delivery techniques have been predominantly used for the management of respiratory ailments such as pneumonia and for evaluating pulmonary ventilation through nuclear medicine imaging. In the clinical setting, intravenous injection is the most common method used for lung cancer immunotherapy. This approach results in the predominant distribution of ICIs, represented by antibodies, in metabolic organs, and only a small amount of ICIs accumulate in the lungs (*16*). In addition, as a type of solid tumor, lung cancer has a wide range of molecular heterogeneity, and the efficacy of monoclonal antibody immunotherapy drugs is limited by their shallow penetration and interactions within the TME. Consequently, higher doses or multiple immunotherapy agents are required to meet therapeutic goals because of the low efficacy of these drugs. Moreover, high immunogenicity may result in severe side effects and high treatment costs (*17*). The respiratory delivery approach allows therapeutic drugs to reach the target more efficiently. The PFC-based NE platform, characterized by its size controllability and inhalation capability through nebulization, enables the deep deposition of therapeutic drugs within the alveoli, facilitating their prolong retention and infiltration at target sites (*18*). The LAG-3–targeting blockade cyclic peptide C25 has suitable tissue and tumor penetration compatibility (*12*, *19*). Therefore, based on the PFC NE platform, we appropriately augmented the C25 loading efficiency, prolonged its retention time, facilitated the efficient distribution of C25 in tumors and TDLNs, and mitigated nontarget organ drug distribution through a nebulization delivery approach. Moreover, the absence of a background signal makes the ^{19}F nucleus a unique and highly attractive biomarker for detecting fluorinated PFCE-C25 NEs in vivo via ^{19}F-MRI. In particular, our observation of PFCE-C25 NEs in TDLNs and subsequent DC and T cell activation at this site may have broad implications for the development of lung cancer immunotherapies.

Jin *et al.* recently demonstrated the immunotherapeutic effects of repeated inhalation of the Chitosan (CS)/aPD-L1 complex on lung metastasis (*20*). However, the mechanism through which immunotherapeutic drugs are distributed in the lungs to achieve effective immunotherapy has not been extensively explored. In our previous study, we found that PFC NEs can quickly and effectively infiltrate into TDLNs. Therefore, we were interested in exploring whether PFCE-C25 NEs could also induce an immune response in TDLNs since the LAG-3 expression level in TDLNs was not lower than that in tumors. As expected, we observed that PFCE-C25 NEs substantially accumulated in TDLNs and induced a significant immune response. In addition to the activation of T cells in the TDLNs, robust DC activation and maturation occur early after (2 hours) PFCE-C25 NE nebulized delivery, as evidenced by the blockade of LAG-3 activity on DC promoted DC maturation and the reactivation of functional $CD4^+/CD8^+$ T cells (*6*). Moreover, the activation of DCs was shown to be sustained for an extended duration, as demonstrated by the prolonged retention and infiltration capabilities of PFCE-C25 NEs. Various tissues, including the tumor, TDLN, and spleen, showed sustained $CD8^+$ and $CD4^+$ T cell infiltration as determined after 6 days of single low-dose PFCE-C25 NE nebulization therapy, in which the ratio of tumor-infiltrating T cells and the proportion of $CD4^+/CD8^+$ IFN-γ^+ T cells in the TDLNs were significantly greater. The apparent efflux of T cells from these tissues inhibits in situ tumor growth and facilitates the abscopal effect of controlling distant tumors. DCs trigger antigen spreading through tissue-resident memory $CD8^+$ T cells to promote tumor antigen–specific immunity (*21*). Consequently, compared with the control group, the PFCE-C25 NE–treated group exhibited substantial amounts of T_{CM} cells ($CD8^+$ $CD44^{high}$ $CD62L^{high}$) and T_{EM} cells ($CD8^+$ $CD44^{high}$ $CD62L^{low}$). Overall, the abundance and function of each effector subset were substantially increased in response to PFCE-C25 NEs not only in the TME but also in the TDLNs, the latter of which might be the key site for the initiation of superior anticancer efficacy in response to PFCE-C25 NEs.

Considering the fundamental differences in immune function between species, we conducted a series of studies on HIS mice and further verified the clinical translational potential of PFCE-C25 NEs. The results highlighted an expected treatment response in HIS mice. Moreover, since the deposition of respiratory-derived PFCE-C25 NEs is confined only to the lung tissues, in addition to the ultimate clearance of PFCE-C25 NEs via exhalation through the lungs, there is no chance of causing toxic side effects on other vital organs of the body. This treatment may help improve the clinical outcomes of patients. The targeting ability and immunological effects of PFCE-C25 NEs were further explored on hTDLNs and hPBMCs, given C25's

specific binding to both human and mouse LAG-3 (*12*). The results demonstrated a significantly higher binding affinity of PFCE-C25 NEs to hTDLNs in comparison to PFCE NEs. Thus, PFCE-C25 NEs potentially have significant clinical application merit. However, additional work needs to be done in this exciting field to fully reveal the clinical benefit of the current research. Another possible future application of PFCE-C25 NEs is the development of engineering strategies for lymph node–targeted immune activation that create optimal lymph node conditions for T cell stimulation and priming. The NK cell and B cell responses in other TDLNs will be the subject of future investigations, as LAG-3 is expressed on multiple immune cells and plays key roles in immune escape by interacting with its ligands. Moreover, immunotherapy studies are mostly carried out during the early stages of tumor development to achieve effective therapeutic effects. Here, single low-dose nebulization delivery effectively impeded the progression of orthotopic tumors and completely halted the growth of distal tumors, exhibiting a remarkable abscopal effect. Clinically, the onset of lung cancer is indistinguishable, raising the question of whether PFCE-C25 NE therapy can benefit patients with more advanced stages of lung cancer. Therefore, investigating the potential of optimizing PFCE-C25 NE nebulization therapy depending on the tumor stage holds promise for enhancing the future applicability of PFCE-C25 NE immunotherapy.

In summary, this study represents a proof of concept for the efficacy of pulmonary nebulized delivery of PFCE-C25 NEs in lung cancer immunotherapy and provides valuable insight into the mechanisms underlying PFCE-C25 NE efficacy. We fully illustrated that a single low-dose nebulization delivery of PFCE-C25 NEs to active lymph nodes blocked LAG-3 activity and provided durable stimulation of systemic antitumor immunity in lung cancer model mice. Notably, the LAG-3 blockade by PFCE-C25 NEs successfully promoted T cell proliferation, facilitated cytokine release, and facilitated DC maturation and $CD8^+$ T cell–derived immune memory. In addition, single low-dose PFCE-C25 NE nebulization therapy not only strongly enhanced LAG-3 blockade efficacy but also greatly inhibited the potential toxicity to other organs. This platform provides advantages over existing delivery technologies in terms of enhanced therapeutic efficacy through pulmonary cancer drug delivery, increased drug penetration in tumors and TDLNs, and real-time visualization of the quantity of immunotherapeutic drugs in the lungs via ^{19}F MRI technology. Overall, this study provides an engineering strategy for a more effective lung cancer immunotherapy, paving the way for a much broader application of anticancer immunotherapy delivered via the pulmonary route and serving as a valuable framework for future research endeavors.

MATERIALS AND METHODS

Reagents, cell lines, and animals

Unless otherwise stated, all of the solvents and reagents were purchased from Aldrich Chemical Co. and used as received. PFCE ($C_{10}F_{20}O_5$) was obtained from Exfluor Research Corporation (Round Rock, TX). Phospholipids were purchased from Avanti Polar Lipids Inc. (Alabama, USA). LLC, CMT167, and NCI-H460 cells were purchased from the American Type Culture Collection (ATCC) and cultured according to ATCC guidelines. NCI-H460 cells were cultured in RPMI 1640 medium supplemented with 10% fetal bovine serum (FBS). LLC and CMT167 lung cancer cells were cultured in Dulbecco's modified Eagle medium (DMEM), supplemented with 10% FBS. All cell lines were cultured at 37°C in a humidified atmosphere with 5% CO_2 and routinely tested for mycoplasma contamination. C57BL/6 N and NOG mice were purchased from Vital River Laboratory Animal Technology Co. Ltd. [certificate number: SCXK (Jing) 2016-0006; Beijing, China], housed in a specific pathogen–free (SPF) barrier facility in groups of four to five per ventilated cage with ad libitum access to food and water, and kept on a 12-hour light/dark cycle. All animal procedures were carried out with the approval (permit 2022-DWSYLLCZ-09) of the Animal Ethics Committee of Harbin Medical University (Harbin, China) and were in agreement with the guidelines of the Institutional Animal Care and Use Committee.

Preparation of PFCE-C25 NEs

Lissamine rhodamine B sulfonyl–labeled PFCE NEs were synthesized using microfluidization, as previously described (*22*). First, the PFCE NEs consisted of 20% (v/v) PFCE and 2% (w/v) amino-rich surfactant, which included 85.9 mol % L-α-phosphatidylcholine (96%) (soy), 3 mol % 1,2-Distearoyl-sn-Glycero-3-Phosphoethanolamine DSPE-polyethylene glycol (PEG)–amine [molecular weight (MW) 2000] (ammonium), 1 mol % 1,2-dipalmitoyl-sn-glycero-3-phosphoethanolamine (DPPE), 10 mol % cholesterol, and 0.1 mol % lissamine rhodamine B sulfonyl (16:0 LissRhod PE). The lipids were dissolved in a mixture of methanol and chloroform, filtered through a small bed of cotton, evaporated under reduced pressure using a rotary evaporator at 45°C to form a thin film, and then further dried in a vacuum oven (45°C) for 24 hours. The resuspended surfactant was combined with PFCE, water, and glycerol and then emulsified in an M110P Microfluidics emulsifier (Microfluidics, Newton, MA) at 20,000 psi for 4 min. The resulting PFCE NEs were the precursors of the PFCE-C25 NEs. Second, MES buffer (pH 6.0, 0.1 mM) containing 1-ethyl-3-(3-dimethylaminopropyl)carbodiimide (EDC) (MW = 191.7) and *N*-hydroxysuccinimide (NHS) (MW = 217.2) in a 2:1 molar ratio was added to C25 cyclic peptide and then added to the PFCE NEs. The mixture was thoroughly mixed and reacted for 1 hour. A condensation reaction occurred between the amino group of the surfactant and the carbonyl group of the C25 cyclic peptide to form the PFCE-C25 NEs. The reaction was terminated by adding ethanolamine. The products were dialyzed against deionized water using a 20-kDa MW cutoff cellulosic membrane to completely remove residual components. The completed emulsions were placed in crimp-sealed vials, blanketed with argon, and stored at 4°C until use.

HPLC analysis

The concentration of the C25 peptide in the PFCE-C25 NEs was determined using HPLC. Specifically, the dialysate of the PFCE-C25 NEs was analyzed using a Gilson GX-281 system (Gilson Technologies, USA) equipped with a C18 column (Phenomenex Kinetex, 5 μm EVO C18, 100 Å, 250 × 4.6 mm). Detection was performed at wavelengths of 220 and 254 nm at room temperature. The mobile phase was composed of (A) 5% acetonitrile in 95% H_2O and (B) 95% acetonitrile in 5% H_2O, with a flow rate of 1 ml/min. The gradient was as follows: 0 to 2 min (isocratic elution, 100% A), 2 to 20 min (gradient elution, A to B), 20 to 30 min (isocratic elution, 100% A). The injection volume of the dialysate was 790 μl. The retention time for C25 was observed to be 12.8 min. The final concentration of C25 was determined to be 1.074 μg/μl. The grafting efficiency (GE) was calculated to be 81.06% using the following formula: GE% = (weight of C25 cyclic peptide grafted on nanoparticles/initial weight of C25 cyclic peptide) × 100%.

Characterization of the PFCE-C25 NEs

The hydrodynamic diameter distribution and ζ potential (ζ) of the PFCE-C25 NEs were determined via DLS with a Malvern Nano ZS Zetasizer (Malvern Instruments Ltd., Malvern, UK) at different temperatures and time intervals. The absorbances of the C25 peptide and lissamine rhodamine B sulfonyl probe was measured using a multiplate UV absorbance spectrophotometer (BioTek, Winooski, VT). The morphology and microstructure of the PFCE-C25 NEs were determined via TEM on a Hitachi 7700 microscope at an accelerating voltage of 80 kV. Briefly, a drop of the sample was deposited on a carbon grid coated with copper, and the excess sample was drawn off with filter paper 1 min later and then left for 5 min for drying. TEM element mapping analysis of the PFCE-C25 NEs was performed using an FEI Talos F200X Super-X SDD detector at an acceleration voltage of 200 kV. Cryo-TEM was performed using Talos F200C 200 kV equipment.

LAG-3–targeting properties of PFCE-C25 NEs

Ex vivo fluorescence imaging experiments were carried out to verify the targeting capacity of the PFCE-C25 NEs. First, mouse spleen single-cell suspensions were prepared as previously described (*23*), and $CD8^+$ T cells were purified from the spleens of C57BL/6 N mice by magnetic cell sorting using mouse CD8 Dynabeads (BioLegend) according to the manufacturer's instructions. The purity of the $CD8^+$ T cells was >95%. Freshly isolated $CD8^+$ T cells were cultured in RPMI supplemented with 10% FBS and stimulated with anti-CD3 (1 mg/ml) (eBioscience) and anti-CD28 (0.5 mg/ml) antibodies (eBioscience). Stimulated or nonstimulated $CD8^+$ T cells were incubated with PFCE-C25 NEs. LAG-3 blocking (Abcam) antibody was also used as the negative control. After 4 hours of incubation with probes, the $CD8^+$ T cells were centrifuged and transferred to poly-L-lysine (PLL)–coated confocal dishes. The cells were allowed to attach for 2 hours, after which the cell nuclei were stained with 4′,6-diamidino-2-phenylindole (DAPI) (Thermo Fisher Scientific). Then, images of the cells were captured by a confocal laser scanning microscope (Nikon, Japan).

hPBMC assay

PBMCs from healthy donors were separated via density gradient centrifugation (Sichuan Hope Biotechnology Co. Ltd., China). hPBMCs (1×10^6 cells per well) were cultured in six-well plates with 2.5 ml of Iscove's Modified Dulbecco's Medium (IMDM) containing 10% FBS. For cytokine flow cytometry analysis, hPBMCs were stimulated with phorbol 12-myristate 13-acetate (PMA) (50 ng/ml) and ionomycin (500 ng/ml) for 6 hours. Then, the activated hPBMCs were incubated with PFCE-C25 NEs (25, 50, and 100 μM based on the C25 peptide) or anti–LAG-3 blocking antibody (5 μg/ml) (Abcam). A protein transport inhibitor cocktail (2.5 μl, BD Biosciences) was added to each well, and the cells were incubated for 4 hours. The cells were collected and stained with the surface marker peridinin chlorophyll protein (PerCP) anti-human CD45 antibody (BioLegend), fluorescein isothiocyanate (FITC) anti-human CD3 antibody (BioLegend), allophycocyanin (APC)/Cyanine7 anti-human CD4 antibody (BioLegend), and phycoerythrin (PE)/Cyanine7 anti-human CD8a antibody (BioLegend) before fixation and permeabilization. Permeabilized cells were then stained with a PE-conjugated anti-human IFN-γ antibody (BioLegend) and analyzed by using a flow cytometer (Beckman Coulter, Fullerton, CA, USA). All the results were analyzed using FlowJo 10.4 software (FlowJo LLC).

hTDLN assay

All experiments using human samples received approval from the Fourth Hospital of Harbin Medical University's ethics committee according to related ethical guidelines, and the patients consented to the research use of biopsy samples (2023-Ethical review-34). The hTDLN biopsy fresh samples were submerged in DMEM (high glucose) medium (LONSERA) containing 10% FBS in a six-well cell culture plate and cocultured with PFCE-C25 NEs or PFCE NEs for 6 hours (5% CO_2, 37°C). Then, hTDLN blocks were collected and subjected to ^{19}F-MRI, IVIS Lumina III imaging, and H&E staining. For IVIS Lumina III imaging studies, the regions of interest (ROIs) were quantified as the average radiant efficiency [p s^{-1} cm^{-2}]/[μW cm^{-2}] by using IVIS Living Image 4.3.1 software. For the flow cytometry assay, the hTDLN tissue was first separated and sectioned into 1-mm^3 samples, which were then incubated with PFCE-C25 NEs or PFCE NEs for 6 hours. Subsequently, the samples were analyzed using flow cytometry to assess the maturation of DCs or the ratio of $CD8^+$ IFN-γ^+ T and $CD4^+$ IFN-γ^+ T cells.

In vitro, ex vivo, and in vivo ^{19}F-MRI studies

In vitro, ex vivo, and in vivo ^{19}F-MR images were acquired on a 9.4-T MRI scanner (Bruker BioSpec 94/20 USR system, Germany). Different concentrations of PFCE-C25 NE phantoms were prepared and subjected to ^{19}F-MRI (181.4, 90.7, 43.35, 22.68, 11.35, and 5.67 g/liter). For ex vivo imaging, hTDLN blocks were collected in Eppendorf (EP) tube and subjected to ^{19}F-MRI. For in vivo imaging, mice were anesthetized by inhalation of an initial dose of 2% isoflurane (RWD Life Science) followed by a continuous dose of 1.5% isoflurane supplied via a nose cone during ^{19}F-MRI. The respiratory rates were continuously monitored by a small-animal monitoring and gating system (SA Instruments), and the body temperature was maintained at 37°C using a temperature-controlled heating system (Thermo Fisher Scientific). The ^{19}F-Relaxation Enhanced Rapid Excitation (RARE) sequence parameters were as follows: Repetition time (TR) = 2000 ms, Echo time (TE) = 100 ms; average: 128; echo spacing: 6.25; rare factor: 32; image size: 64 × 64; and field of view: 38.4 × 38.4. The SNR of each sample/mouse was calculated via Pravision 6.0.1 system software.

The retention of PFCE-C25 NEs in the lungs, tumors, and TDLNs

To test whether the PFCE-C25 NEs could be uniformly distributed in the lungs, we used lissamine B sulfonyl–labeled PFCE-C25 NEs to visualize the distribution of PFCE-C25 NEs in the lungs, tumors, and TDLNs. Specifically, a nebulized delivery method was used to administer C25 peptide–based PFCE-C25 NEs (1.074 μg/μl) in a liquid volume of 50 μl to an in situ LLC mouse model. Then, the lungs and TDLNs were collected for fluorescence imaging 6 hours after PFCE-C25 NE delivery. Cell nuclei were stained with DAPI (Thermo Fisher Scientific). Images of the tissues were captured by a confocal laser scanning microscope (Nikon, Japan).

Establishment of in situ lung cancer mouse models

For the in situ LLC model, LLC cells (1×10^6 cells/ml, 200 μl) were intravenously injected into 6-week-old female C57BL/6 N mice. For the CMT167 orthotopic lung cancer model, 2×10^5 CMT167 lung cancer cells were suspended in PBS and Matrigel solution (PBS:Matrigel = 1:1), and 50 μl of cell suspension was injected into the lung tissue in the third and fourth intercostal spaces on the right side of 6-week-old

female C57BL/6 N mice. Animals were anesthetized using 1.5% isoflurane administered via a nose cone mask. For the humanized mouse model of NCI-H460 orthotopic lung cancer, NCI-H460 cells (1×10^7 cells/ml, 50 μl) were delivered into the mouse main bronchus with the assistance of a mouse laryngoscope (Penn-Century Inc.). Mice were closely monitored until they recovered from anesthetization and subsequently transferred back to standardized animal care. After 3 days of tumor inoculation, 5×10^6 hPBMCs were injected into each NOG mouse to establish a humanized lung cancer mouse model. Peripheral blood from all mice was monitored for T cell (PerCP anti-human CD45 antibody, FITC anti-human CD3 antibody, BioLegend) reconstitution. Twelve days after hPBMC transplantation, mice harboring similar percentages of $hCD45^+$ $hCD3^+$ cells (>20%) were selected for treatment assessment. T_1WI was performed on a 9.4-T MRI scanner (Bruker BioSpin 94/20 USR system, Germany), and the successful establishment of the above in situ lung cancer models was confirmed.

In vivo treatment and antitumor efficacy monitoring

After successful establishment of in situ lung cancer mouse models, the mice were randomly grouped and treated as follows: (i) PFCE-C25 NEs (2.685 mg/kg per single dose, based on C25 peptide, intratracheally), (ii) C25 peptide (2 mg/kg per day, intraperitoneally), (iii) LAG-3 antibody (10 mg/kg per every 3 days, intraperitoneally), and (iv) PBS (every 3 days, intraperitoneally). The C25 peptide and LAG-3 antibody were used as the positive control, while PBS was used as the negative control. The therapeutic effects of a single low dose of PFCE-C25 NEs were compared with those of the C25 peptide, LAG-3 antibody, and PBS groups. Overall survival was assessed for 28 days after treatment initiation. Tumor growth was monitored by using a 9.4-T MRI scanner. MRI was performed on day 0 and subsequently performed on days 4, 10, and 14. Anatomical T1-weighted imaging was conducted using a RARE sequence with TR = 820 ms, TE = 12 ms; average: 4; echo spacing: 6; rare factor: 8; image size: 256 × 256; and field of view: 38.4 × 38.4. The body weights of the mice were observed every 2 days. The subcutaneous tumor size was measured by calipers, and the tumor volume was calculated via the following formula: Volume (mm^3) = Long diameter × (short diameter) 2/2. Lungs and sera were collected on the sixth day after treatment for further evaluation. Tumor sections collected from different groups of mice were stained with H&E on day 14. On day 39 after 14 days of treatment, complete tumor elimination after receiving PFCE-C25 NEs was further abrogated by reinjection of the same tumor cell line, after which the mice were tested for tumor-specific immune memory, as measured by the rate of tumor growth in rechallenged mice compared to age-matched naïve control mice. The C25 cyclic peptide was synthesized and provided by Shanghai Science Peptide Biological Technology Co. Ltd. (China). Therapeutic anti-mouse or human LAG-3 antibodies were purchased from BioXCell (USA).

Validation of therapeutic efficiency by flow cytometry

Flow cytometry was performed as previously described (*12*, *14*, *24*). Briefly, tumors, TDLNs, and spleens were harvested from mice in each treatment group on the sixth day after treatment, homogenized in cold FACS (fluorescence-activated cell sorting) buffer solution (1% FBS in PBS), and passed through a 70-mm cell strainer to obtain a single-cell suspension. Tumor tissues were minced and digested in collagenase IV (Solarbio) and deoxyribonuclease I (Solarbio) for 1 hour at 37°C. Single-cell suspensions were stained with a fluorescence-labeled PerCP-conjugated anti-mouse CD45 antibody (BioLegend), a FITC-conjugated anti-mouse CD3 antibody (BioLegend), an APC-conjugated anti-mouse CD4 antibody (BioLegend), a PE-conjugated anti-mouse CD8a antibody (BioLegend), and a PE-conjugated anti-mouse intracellular IFN-γ staining antibody (BioLegend) to assess the tumor, spleen, and TDLN-infiltrating lymphocyte status, as well as IFN-γ expression. The APC/Cyanine7-conjugated anti-mouse CD4 antibody (BioLegend) and PE/Cyanine7-conjugated anti-mouse CD25 antibody (BioLegend) were applied before fixation and permeabilization. Permeabilized cells were then stained with a PE-conjugated anti-mouse nuclear FOXP3 antibody (BioLegend) to evaluate the proportion of T_{regs} ($CD4^+CD25^+Foxp3^+$) in tumor tissue. An APC-conjugated anti-mouse CD223 (LAG-3) antibody was used to confirm the LAG-3 expression levels in the LLC and CMT167 lung cancer mouse models. For the HIS NCI-H460 orthotopic lung cancer model, PerCP-conjugated anti-human CD45 antibody (BioLegend), FITC-conjugated anti-human CD3 antibody (BioLegend), APC-conjugated anti-human CD4 antibody (BioLegend), and PE-conjugated anti-human CD8a antibody (BioLegend) were used to assess the infiltrating lymphocytes in the tumors and TDLNs. An APC-conjugated anti-human CD223 (LAG-3) antibody (BioLegend) was used to determine LAG-3 expression in the HIS NCI-H460 orthotopic lung tumors. Fc blocking was performed by staining sections with anti-CD16/32 (BioLegend) to avoid nonspecific binding. Doublets and debris were excluded before various gating strategies were applied. Dead cells were excluded using Zombie Red viability dye (BioLegend). For MHC-I and MHC-II expression analysis, Zombie NIR Fixable viability Kit was used to exclude dead cells. The FITC-conjugated anti-mouse CD45, APC-conjugated anti-mouse CD11c, PerCP/Cyanine5.5-conjugated anti-mouse I-A/I-E, and PerCP/Cyanine7-conjugated anti-mouse H-2Kb/H-2Db were used to assess the infiltrating DCs in the tumors and TDLNs and the expression of MHC-I and MHC-II on DCs. Gating was generated based on fluorescence minus one (FMO) control staining. After staining, 1.0×10^6 cells in each sample were washed and analyzed by using a flow cytometer (Beckman Coulter, Fullerton, CA, USA). All of the results were analyzed using FlowJo 10.4 software (FlowJo LLC). Exemplifying flow cytometry gating strategy was demonstrated in figs. S23 to S26.

DC maturation state testing

After a single low-dose nebulization delivery of PFCE-C25 NEs (2.685 mg/kg based on the C25 peptide, single dose, intratracheally), TDLNs were obtained from LLC mice model at 2 hours and 6 days after administration. The C25 peptide group was used as a control after a single administration (2 mg/kg, intraperitoneally). For the flow cytometry assay, DCs in TDLNs were stained with FITC-conjugated anti-mouse CD11c antibody, PE-conjugated anti-mouse CD86 antibody, and APC-conjugated anti-mouse CD80 antibody and detected by using a flow cytometer (Beckman Coulter, Fullerton, CA, USA); the results were analyzed using FlowJo 10.4 software (FlowJo LLC). To assess DC maturation using immunofluorescence, TDLN slides were fixed with 4% paraformaldehyde for 15 min and rinsed with PBS. The slides were then exposed to SuperBlock (PBS) blocking buffer (Thermo Fisher Scientific) at room temperature for 30 min and incubated thereafter with primary antibodies against CD80 and CD86 (Thermo Fisher Scientific) in SuperBlock blocking buffer at 1:100 dilutions overnight at 4°C. The cells were then washed three times with PBS and incubated in SuperBlock blocking buffer with Alexa Fluor 594–conjugated anti-mouse secondary antibody

(1:500 dilutions; Thermo Fisher Scientific) and Alexa Fluor 488–conjugated anti-rabbit secondary antibody (1:500 dilutions; Thermo Fisher Scientific) for 1 hour at room temperature. Cell nuclei were stained with DAPI for 5 min at room temperature. Images of the cells were captured by a confocal laser scanning microscope (Nikon, Japan). Exemplifying flow cytometry gating strategy was demonstrated in fig. S27.

Depletion of T cells

C57BL/6 N mice were inoculated with LLC cells and divided into four groups [treated, CD4 depletion, CD8a depletion, and untreated (UnTx)]. On days 8 and 11, the mice were injected intravenously with anti-CD4 (20 μg per mouse, BioXCell) and anti-CD8a (20 μg per mouse, BioXCell), respectively. Next, on day 12, PBMCs were collected to analyze the efficiency of T cell (including $CD4^+CD8a^+$) depletion. On the same day, the mice were treated with PFCE-C25 NEs, except for UnTx.

Tumor-specific immune memory

For the tumor rechallenge assay, seven healthy mice and five mice cured via PFCE-C25 NEs were intravenously injected with LLC cells (2×10^5) 39 days after the first round of treatment. Twenty-two days after tumor inoculation, the populations of T_{CM} cells ($CD8^+$ $CD44^{high}$ $CD62L^{high}$) and T_{EM} cells ($CD8^+$ $CD44^{high}$ $CD62L^{low}$) in the sera collected from these cured mice and healthy mice were analyzed via flow cytometry. T_{CM} and T_{EM} cells in the serum were stained with a PerCP/Cy5.5 anti-mouse CD8 antibody (BioLegend), a PE-conjugated anti-mouse CD44 antibody (BioLegend), and an APC-conjugated anti-mouse CD62L antibody (BioLegend) and were observed by flow cytometry (Beckman Coulter, Fullerton, CA, USA); the results were analyzed using FlowJo 10.4 software (FlowJo LLC). To investigate tumor-specific immune memory using immunofluorescence staining, TDLN slides were fixed with 4% paraformaldehyde for 15 min and rinsed with PBS. The slides were then exposed to SuperBlock (PBS) blocking buffer (Thermo Fisher Scientific) at room temperature for 30 min and incubated thereafter with the $CD8^+$ and CD44 primary antibodies (Thermo Fisher Scientific) in SuperBlock blocking buffer at 1:100 dilutions overnight at 4°C. The tissue slides were then washed three times with PBS and incubated in SuperBlock blocking buffer with Alexa Fluor 594–conjugated anti-rabbit secondary antibody (1:500 dilution; Thermo Fisher Scientific) and Alexa Fluor 488–conjugated anti-rat secondary antibody (1:500 dilution; Thermo Fisher Scientific) for 1 hour at room temperature. Cell nuclei were stained with DAPI for 5 min at room temperature. Images of the cells were captured by a confocal laser scanning microscope (Nikon, Japan). Lung tissue sections were stained with H&E.

Cytokine evaluation

On day 6, serum and tumor tissues were collected for cytokine analysis using ELISA. The tumor tissues were homogenized in lysis buffer, transferred to microtubes, and centrifuged at 13,200*g* for 10 min. The supernatants were subsequently transferred to fresh microtubes. The concentrations of interleukin-6 (IL-6), IL-12, TNF-α, and IFN-γ in the supernatants and blood samples were measured with ELISA kits (BioLegend) according to the manufacturer's instructions. The optical densities were determined at wavelengths of 450 and 570 nm using an ELISA plate reader (BioTek, Winooski, VT).

Biological safety evaluation

After the single low-dose administration of PFCE-C25 NEs (2.685 mg/kg based on the C25 peptide, single dose, intratracheally), C25 peptide (2 mg/kg, intraperitoneally), LAG-3 antibody (10 mg/kg, intraperitoneally), and PBS (intraperitoneally) for 14 days, all C57BL/6 N mice were sacrificed and their heart, liver, spleen, kidney, lung, muscle, and intestine were removed, washed with cold saline, and fixed with 10% formaldehyde at 4°C for at least 24 hours through perfusion. Next, the organs were sectioned and embedded in paraffin blocks for H&E staining. The histological sections were examined under a microscope (OLYMPUS, Japan) at ×20 magnification. Furthermore, blood biochemical indices were measured to evaluate the cumulative effect of PFCE-C25 NEs. Female BALB/c mice aged 6 weeks were selected for routine blood tests and biochemical assays, and control mice were injected with saline. After 7 and 45 days of treatment, blood samples were collected from the eye sockets of the mice and analyzed via a hematology analyzer.

Biodistribution study

Initially, PFCE-C25 NEs (2.685 mg/kg based on the C25 peptide, single dose, intratracheally) were administered via nebulization to healthy C57BL/6 N mice. Then, the mice were sacrificed 1, 3, 7, and 14 days after nebulization delivery of PFCE-C25 NEs. Tumors and main organs were collected and subjected to fluorescence measurements for lissamine rhodamine B sulfonyl via the IVIS Lumina III imaging system (Caliper Life Science, USA). The ROIs were quantified as the average radiant efficiency [p s^{-1} cm^{-2}]/[μW cm^{-2}] by using IVIS Living Image 4.3.1 software.

The quantification of C25 peptide content in tumor tissues and normal organs was conducted using HPLC at specific time intervals of 2 hours, 1 day, 6 days, and 14 days after injection (intraperitoneally). The lungs, tumors, and major immune and metabolic organs (TDLNs, livers, spleens, intestines, and kidneys) were collected and weighed before the measurements were taken. Additionally, the PFCE concentration in tumor tissues and normal organs was measured via ^{19}F-NMR after nebulization delivery of 50 μl of PFCE-C25 NEs. Tissues were collected, homogenized in lysis buffer, transferred to tubes, and centrifuged for 20 min at 13.2 × 1000*g*. Then, D_2O (Sigma-Aldrich, Germany) and 0.1% (w/v) CF_3COONa (Macklin, China) internal reference were added to the supernatants. Then, the samples were subjected to ^{19}F-NMR measurements by using a Broadband Frequency Offset (BBFO) probe, for which the parameters consisted of 32 scans and a 2-μs delay.

Cell cytotoxicity assay

MTT assay was used to assess in vitro cytotoxicity. LLC, CMT167, and NCI- H460 cancer cells were seeded in a 96-well plate at a density of 5×10^3 per well and then cultured in 5% CO_2 at 37°C for 24 hours. The serum-free culture media were replaced with PFCE-C25 NEs at 0, 12.5, 25, 50, 100, and 200 μM. After further incubation at 37°C and 5% CO_2 for 24 or 48 hours, the culture media were removed and washed with PBS twice. Then, 120 μl of MTT DMEM or RPMI 1640 solution (0.8 mg/ml) was added to cells and incubated for 4 hours. Finally, the MTT media were replaced with dimethyl sulfoxide (DMSO; 150 μl per well). Absorbance was monitored using a microplate reader (BioTek, USA) at a wavelength of 490 nm, and cytotoxicity was expressed as the percentage of cell viability compared to control cells.

Statistical analysis

All studies were repeated at least three times or measured in triplicate. The results are reported as the means ± SD. Student's *t* test was used

for two-group comparisons. One-way analysis of variance (ANOVA) was used to determine the statistical significance of differences between more than two groups. For comparisons among multiple groups, two-way ANOVA was used. For animal survival analysis, the significant differences were determined by the log-rank test. The results were significant when ****$P < 0.0001$, ***$P < 0.005$, **$P < 0.01$, and *$P < 0.05$. All of the statistical analyses were performed with GraphPad Prism 8.4.0 software (GraphPad Software, CA).

Supplementary Materials

This PDF file includes:

Figs. S1 to S27

REFERENCES AND NOTES

1. D. Xiang, S. Hu, T. Mai, X. Zhang, L. Zhang, S. Wang, K. Jin, J. Huang, Worldwide cancer statistics of adults over 75 years old in 2019: A systematic analysis of the global burden of disease study 2019. *BMC Public Health* **22**, 1979 (2022).
2. H. du Bois, T. A. Heim, A. W. Lund, Tumor-draining lymph nodes: At the crossroads of metastasis and immunity. *Sci. Immunol.* **6**, eabg3551 (2021).
3. B. Liang, C. Workman, J. Lee, C. Chew, B. M. Dale, L. Colonna, M. Flores, N. Li, E. Schweighoffer, S. Greenberg, V. Tybulewicz, D. Vignali, R. Clynes, Regulatory T cells inhibit dendritic cells by lymphocyte activation gene-3 engagement of MHC class II. *J. Immunol.* **180**, 5916–5926 (2008).
4. F. Aroldi, R. Saleh, I. Jafferji, C. Barreto, C. Saberian, M. R. Middleton, Lag3: From bench to bedside. *Cancer Treat. Res.* **183**, 185–199 (2022).
5. L. P. Andrews, A. E. Marciscano, C. G. Drake, D. A. Vignali, LAG3 (CD223) as a cancer immunotherapy target. *Immunol. Rev.* **276**, 80–96 (2017).
6. J.-L. Huo, Y.-T. Wang, W.-J. Fu, N. Lu, Z.-S. Liu, The promising immune checkpoint LAG-3 in cancer immunotherapy: From basic research to clinical application. *Front. Immunol.* **13**, 956090 (2022).
7. T. Maruhashi, D. Sugiura, I. M. Okazaki, T. Okazaki, LAG-3: From molecular functions to clinical applications. *J. Immunother. Cancer* **8**, e001014 (2020).
8. S. H. van Rijt, T. Bein, S. Meiners, Medical nanoparticles for next generation drug delivery to the lungs. *Eur. Respir. J.* **44**, 765–774 (2014).
9. S. S. Kunde, R. Ghosh, S. Wairkar, Emerging trends in pulmonary delivery of biopharmaceuticals. *Drug Discov. Today* **27**, 1474–1482 (2022).
10. A. H. J. Staal, K. Becker, O. Tagit, N. Koen van Riessen, O. Koshkina, A. Veltien, P. Bouvain, K. R. G. Cortenbach, T. Scheenen, U. Flogel, S. Temme, M. Srinivas, In vivo clearance of (19) F MRI imaging nanocarriers is strongly influenced by nanoparticle ultrastructure. *Biomaterials* **261**, 120307 (2020).
11. H. Wang, X. Li, J. Wang, J. Wang, H. Zou, X. Hu, L. Yang, P. Shen, R. A, K. Wang, Y. Li, J. Yang, K. Wang, L. Yang, L. Wu, X. Sun, Alveolar macrophages-mediated translocation of intratracheally delivered perfluorocarbon nanoparticles to achieve lung cancer ^{19}F-MR imaging. *Nano Lett.* **23**, 2964–2973 (2023).
12. W. Zhai, X. Zhou, H. Wang, W. Li, G. Chen, X. Sui, G. Li, Y. Qi, Y. Gao, A novel cyclic peptide targeting LAG-3 for cancer immunotherapy by activating antigen-specific CD8(+) T cell responses. *Acta Pharm. Sin. B* **10**, 1047–1060 (2020).
13. H. Jiang, H. Ni, P. Zhang, X. Guo, M. Wu, H. Shen, J. Wang, W. Wu, Z. Wu, J. Ding, R. Tang, S. Zhou, B. Chen, M. Yu, H. Jing, J. Liu, PD-L1/LAG-3 bispecific antibody enhances tumor-specific immunity. *Onco. Targets. Ther.* **10**, 1943180 (2021).
14. J. Xu, Q. Ma, Y. Zhang, Z. Fei, Y. Sun, Q. Fan, B. Liu, J. Bai, Y. Yu, J. Chu, J. Chen, C. Wang, Yeast-derived nanoparticles remodel the immunosuppressive microenvironment in tumor and tumor-draining lymph nodes to suppress tumor growth. *Nat. Commun.* **13**, 110 (2022).
15. R. E. Mebius, G. Kraal, Structure and function of the spleen. *Nat. Rev. Immunol.* **5**, 606–616 (2005).
16. J. Chana, B. Forbes, S. A. Jones, Triggered-release nanocapsules for drug delivery to the lungs. *Nanomedicine* **11**, 89–97 (2015).
17. M. C. Bellavia, R. B. Patel, C. J. Anderson, Combined targeted radiopharmaceutical therapy and immune checkpoint blockade: From preclinical advances to the clinic. *J. Nucl. Med.* **63**, 1636–1641 (2022).
18. H. Wang, L. Wu, X. Sun, Intratracheal delivery of nano- and microparticles and hyperpolarized gases: A promising strategy for the imaging and treatment of respiratory disease. *Chest* **157**, 1579–1590 (2020).
19. N. Qvit, S. J. S. Rubin, Peptide therapeutics: Scientific approaches, current development trends, and future directions. *Curr. Top. Med. Chem.* **20**, 2903 (2020).
20. Q. Jin, W. Zhu, J. Zhu, J. Zhu, J. Shen, Z. Liu, Y. Yang, Q. Chen, Nanoparticle-mediated delivery of inhaled immunotherapeutics for treating lung metastasis. *Adv. Mater.* **33**, 2007557 (2021).
21. E. Menares, F. Galvez-Cancino, P. Caceres-Morgado, E. Ghorani, E. Lopez, X. Diaz, J. Saavedra-Almarza, D. A. Figueroa, E. Roa, S. A. Quezada, A. Lladser, Tissue-resident memory CD8$^+$ T cells amplify anti-tumor immunity by triggering antigen spreading through dendritic cells. *Nat. Commun.* **10**, 4401 (2019).
22. A. H. Schmieder, P. M. Winter, T. A. Williams, J. S. Allen, G. Hu, H. Zhang, S. D. Caruthers, S. A. Wickline, G. M. Lanza, Molecular MR imaging of neovascular progression in the Vx2 tumor with $\alpha_v\beta_3$-targeted paramagnetic nanoparticles. *Radiology* **268**, 470–480 (2013).
23. L. Sanchez-Felipe, T. Vercruysse, S. Sharma, J. Ma, V. Lemmens, D. Van Looveren, M. P. Arkalagud Javarappa, R. Boudewijns, B. Malengier-Devlies, L. Liesenborghs, S. J. F. Kaptein, C. De Keyzer, L. Bervoets, S. Debaveye, M. Rasulova, L. Seldeslachts, L. H. Li, S. Jansen, M. B. Yakass, B. E. Verstrepen, K. P. Boszormenyi, G. Kiemenyi-Kayere, N. van Driel, O. Quaye, X. Zhang, S. Ter Horst, N. Mishra, W. Deboutte, J. Matthijnssens, L. Coelmont, C. Vandermeulen, E. Heylen, V. Vergote, D. Schols, Z. Wang, W. Bogers, T. Kuiken, E. Verschoor, C. Cawthorne, K. Van Laere, G. Opdenakker, G. Vande Velde, B. Weynand, D. E. Teuwen, P. Matthys, J. Neyts, H. Jan Thibaut, K. Dallmeier, A single-dose live-attenuated YF17D-vectored SARS-CoV-2 vaccine candidate. *Nature* **590**, 320–325 (2021).
24. R. B. Patel, R. Hernandez, P. Carlson, J. Grudzinski, A. M. Bates, J. C. Jagodinsky, A. Erbe, I. R. Marsh, I. Arthur, E. Aluicio-Sarduy, R. N. Sriramaneni, W. J. Jin, C. Massey, A. L. Rakhmilevich, D. Vail, J. W. Engle, T. Le, K. Kim, B. Bednarz, P. M. Sondel, J. Weichert, Z. S. Morris, Low-dose targeted radionuclide therapy renders immunologically cold tumors responsive to immune checkpoint blockade. *Sci. Transl. Med.* **13**, eabb3631 (2021).

Acknowledgments

Funding: This work was supported by the National Natural Science Foundation of China (81627901 to X.S., 82202226 to Z.H., 82402212 to R.A., and 82400582 to C.N.), the Natural Science Foundation of Heilongjiang Province (grant nos. JQ2020H002 to X.S. and LH2022H034 to Z.H.), the Tou-Yan Innovation Team Program of the Heilongjiang Province (2019-15 to X.S.), the Health Commission of Heilongjiang Province Science and Technology Program (20220909041085 to Z.H.), the Heilongjiang Provincial Key Laboratory of Molecular Imaging Foundation (to X.S.), the China Postdoctoral Science Foundation (2023M740765, 2024T170184, and GZB20240172 to R.A.), and the Guangdong Basic and Applied Basic Research Foundation (2023A1515110304 to R.A.). **Author contributions:** R.A., X.S., Z.H., and Z.Q. contributed to conceptualization, investigation, and methodology. R.A., X.S., and M. Zhou contributed to data curation, resources, validation, visualization, writing—original draft, writing—review and editing, and approval. X.S., Z.H., and R.A. contributed to funding acquisition, supervision, and formal analysis. M. Zhou and C.N. assisted with the preparation of PFCE-C25 NEs and the in vivo MRI studies. C.N. and K.W. assisted with establishing the animal models and conducting in vivo nebulization immunotherapy. Jing Wang, Z.Q., X.H., and Y.W. contributed to human immune system construction. S.L., S.C., M. Zhu, and T.W. assisted with the collection of flow cytometry data. R.A. and H.W. performed the H&E and immunofluorescence staining. Jiannan Wang contributes to verification of the overall replication/reproducibility of experimental results. The final draft of the manuscript was approved by all the coauthors. X.S. conceived the project and supervised the whole research. **Competing interests:** The authors declare that they have no competing interests. **Data and materials availability:** All data needed to evaluate the conclusions in the paper are present in the paper and/or the Supplementary Materials.

Submitted 10 April 2024
Accepted 25 October 2024
Published 29 November 2024
10.1126/sciadv.adp7561